The Dynamics of Unlikely Slip: 3D Modeling of Low-angle Normal Fault Rupture at the Mai'iu Fault, Papua New Guinea

J. Biemiller[1], A.-A. Gabriel[2,1], and T. Ulrich[2]

[1] Institute of Geophysics and Planetary Physics, Scripps Institution of Oceanography, University of California San Diego, La Jolla, California, USA.

[2] Department of Earth and Environmental Sciences, Ludwig Maximillian University of Munich, Munich, Germany.

Corresponding author: James Biemiller (jbiemiller@ucsd.edu)

Key Points:

- We perform the first 3D dynamic rupture simulations of low-angle normal fault earthquake scenarios constrained by laboratory & field evidence
- Large low-angle normal fault earthquakes are dynamically viable under various stress conditions including perfectly Andersonian extension
- Shallow slip is limited by the stabilizing effects of shallow fault geometry, velocity-strengthening gouges, and free-surface interactions

Abstract

Despite decades-long debate over the mechanics of low-angle normal faults dipping less than 30°, many questions about their strength, stress, and slip remain unresolved. Recent geologic and geophysical observations have confirmed that gently-dipping detachment faults can slip at such shallow dips and host moderate-to-large earthquakes. Here, we analyze the first 3D dynamic rupture models to assess how different stress and strength conditions affect rupture characteristics of low-angle normal fault earthquakes. We model observationally constrained spontaneous rupture under different loading conditions on the active Mai'iu fault in Papua New Guinea, which dips 16-24° at the surface and accommodates ~8 mm/yr of horizontal extension. We analyze four distinct fault-local stress scenarios: 1) Andersonian extension, as inferred in the hanging wall; 2) back-rotated principal stresses inferred paleopiezometrically from the exhumed footwall; 3) favorably rotated principal stresses well-aligned for low-angle normal-sense slip; and 4) Andersonian extension derived from depth-variable static fault friction decreasing towards the surface. Our modeling suggests that subcritically stressed detachment faults can host moderate earthquakes within purely Andersonian stress fields. Near-surface rupture is impeded by free-surface stress interactions and dynamic effects of the gently-dipping geometry and frictionally stable gouges of the shallowest portion of the fault. Although favorably-inclined principal stresses have been proposed for some detachments, these conditions are not necessary for seismic slip on these faults. Our results demonstrate how integrated geophysical and geologic observations can constrain dynamic rupture model parameters to develop realistic rupture scenarios of active faults that may pose significant seismic and tsunami hazards to nearby communities.

Plain Language Summary

Movement across faults allow parts of the Earth's crust to move past each other in response to forces driven by tectonic plate motions and can occur during large, devastating earthquakes. The orientation of a fault relative to the direction of the forces and stresses loading determines how easily it can 'slip' in any given direction and whether it will continue to slip or if new fractures and faults will form instead. Some faults appear to be geometrically misoriented and thus 'locked' relative to their local forces, but nonetheless continue to move on the scale of mm per year and accommodate crustal motions. Here, we develop data-constrained computer models to test how different forces at depth affect the movement and associated potential earthquake magnitude of one of these misoriented faults: the Mai'iu normal fault in Papua New Guinea. Our results suggest these faults can indeed slip in large earthquakes under tectonic crustal stress conditions, and that locally favorably rotated stresses would generate even larger earthquakes. We find that seismic slip does not always reach the Earth's surface and explore various physical mechanisms limiting near-surface slip on these faults.

1 Introduction

1.1 Active Low Angle Normal Faults

Normal-sense slip on shallowly-dipping (<30°) detachment faults has helped accommodate tens of kilometers of geologically recorded localized extension in a variety of rift settings (e.g., Collettini et al., 2011). The mechanics of these low-angle normal faults (LANFs) have been extensively debated because such shallowly dipping normal faults appear to defy classic fault mechanical theory. Anderson-Byerlee frictional fault reactivation theory predicts that extension of crustal rocks with Byerlee friction ($0.6 \leq$ static friction coefficient, $\mu_s \leq 0.85$) in an Andersonian stress field (characterized by one vertical principal stress direction) should form normal faults dipping 60-75° and that these faults should frictionally lock up and stop slipping if rotated to dips less than 30° (e.g., Sibson, 1990).

Despite the global abundance of LANFs (Wernicke, 1995; Axen, 2004; Collettini, 2011), the 2010 M_w 7.2 El Mayor-Cucapah earthquake in Mexico was potentially the first instrumentally recorded $M_w > 7$ earthquake to involve coseismic rupture of a LANF (Fletcher et al., 2014, 2016). Understanding the seismogenic potential of LANFs has been complicated by the scarcity of active LANFs and the paucity of instrumentally recorded large ($M_w > 7$) normal-sense earthquakes with well-resolved shallowly-dipping focal mechanisms (Jackson & White, 1989; Wernicke, 1995; Collettini & Sibson, 2001; Collettini, 2011); however, active LANFs slipping up to 1 cm/yr are now well-documented (Webber et al., 2018). Moreover, recent neotectonic (Hayman et al., 2003; Numelin et al., 2007a; Little et al., 2019; Cummins et al., 2020; Biemiller et al., 2020a), seismological (Abers et al., 1997; Abers, 2001; Fletcher et al., 2014, 2016), and geodetic (Anderlini et al., 2016; Biemiller et al., 2020b) evidence from both ancient and active LANFs suggest that these fault systems can host moderate-to-large M_w >7 earthquakes. These earthquakes involve coseismic slip on shallowly dipping segments, despite the abundance of velocity-strengthening gouges in the youngest and shallowest portions of exhumed LANF cores (Numelin et al., 2007b; Smith & Faulkner, 2010; Niemeijer & Collettini, 2014; Mizera et al., 2020; Biemiller et al., 2020b).

Regardless of their tectonic and mechanical origins, active LANFs may pose significant seismic hazards to nearby communities due to the possibility of strong ground motion, landslides, and/or tsunamis associated with large LANF earthquakes (e.g., Cummins et al., 2020). Further constraints on the physics of LANF earthquakes and the mechanical conditions promoting shallow coseismic slip are needed to improve estimates of the seismic hazard potential of these faults. Here, we develop data-constrained 3D numerical dynamic rupture models of a well-documented active LANF, the Mai'iu normal fault in Papua New Guinea. Although the Mai'iu fault has not hosted any large earthquakes during the modern instrumental record, it is one of the best-documented active LANFs in the world that demonstrably dips <30°

at the surface. The local coral paleoseismologic record suggests it hosts infrequent M_w 7.0+ earthquakes. Recent targeted studies provide a wealth of geologic and geophysical observations illuminating the strength, stress, structure and deformation of the Mai'iu fault (Figures 1 & 2), providing the necessary ingredients (section 2) for realistic data-constrained dynamic rupture models that are missing from other proposed seismogenic LANFs like the submarine Moresby Seamount fault (Abers, 2001) and Banda detachment (Cummins et al., 2020) or the buried LANF segment inferred to have slipped during the 2010 El Mayor-Cucapah earthquake (Fletcher et al., 2016). In addition, low-angle slip in modern LANF earthquake candidates remains contested: for example, geodetic (Gonzalez-Ortega et al., 2014) and dynamic rupture (Kyriakopoulos et al., 2017) models explain many features of the 2010 El-Mayor Cucapah event with slip on only steeply-dipping normal faults and no slip on the underlying LANF inferred by Fletcher et al. (2016). Thus, despite the absence of modern large earthquakes, the well-studied Mai'iu fault is one of the best candidates for data-constrained dynamic rupture models of LANF ruptures.

We characterize the dynamics and kinematics of LANF earthquake scenarios and investigate stress and strength conditions that promote or inhibit seismic slip on these faults. In particular, we examine rupture scenarios arising from geologically and geophysically inferred loading and fault strength conditions. We find that such constrained 3D simulations generate surface displacements similar to those recorded paleoseismically. We specifically analyze the factors controlling whether coseismic slip penetrates the shallow velocity-strengthening region during large LANF earthquakes.

1.2 Static and dynamic strength and loading of seismogenic LANFs

The 3D states of stress and effective fault strengths allowing seismic or aseismic LANF activity are difficult to quantify and heavily debated (e.g., Yin, 1989; Spencer & Chase, 1989; Yin et al, 1992; Axen, 1992, 2004, 2020; Buck, 1993; Wernicke, 1995; Abers et al., 1997; Collettini & Sibson, 2001; Westaway, 2005; Collettini, 2011). Major outstanding questions include; Are LANFs actually misoriented for slip, or does fault weakness explain the apparent mechanical paradox? Can LANFs remain active under Andersonian conditions, or do they require rotated principal stresses? Do shallow normal fault dips reflect low static frictional strength, or can LANFs form in strong crust and retain their strength? Are seismogenic LANFs critically stressed, or can sub-critically stressed segments rupture coseismically?

Dynamic rupture models provide self-consistent earthquake descriptions by simultaneously simulating the physical processes that govern fault yielding, coseismic slip, and seismic wave propagation. Data-integrated dynamic earthquake analysis can complement data-driven approaches including complex and/or poorly instrumented events in various tectonic contexts (e.g., Olsen et al., 1997; Douilly et al., 2015; Kyriakopoulos et al., 2017; Wollherr et al.,

2019) to explore the physical conditions and processes behind enigmatic slip behaviors observed in recent earthquakes (e.g., Ulrich et al., 2019b, 2022, Palgunadi, 2020), as well as to develop and test realistic rupture scenarios for active faults that lack a modern record of large earthquakes (e.g., Aochi & Ulrich, 2015; Ramos et al., 2021), which can inform seismic hazard assessment.

In this framework, faults can be stressed well below failure (with a ratio of shear to normal stress, τ/σ_n, lower than static friction μ_s) almost everywhere along the fault, yet break spontaneously. Only a small portion of the fault needs to reach failure to nucleate a rupture, and slip can propagate into regions of velocity- or slip-strengthening frictional behavior (e.g., Thomas et al., 2009; Kaneko et al., 2010) depending on the patterns of static and dynamic stress transfer arising from the initial fault prestress and frictional properties (e.g., Rundle et al., 1984; Cochard & Madariaga, 1996; Ariyoshi et al., 2009). However, few dynamic rupture models exist for normal fault earthquakes and these are restricted to planar faults (Oglesby et al., 1998, 2000, 2008; Aochi, 2018; Gallovic et al., 2019; Aochi & Twardzik, 2020; Tinti et al., 2021); to the best of our knowledge dynamic rupture models have not been used to explore conditions allowing LANF rupture.

Various mechanisms have been proposed to explain how LANFs remain mechanically viable (e.g., Axen, 1992, 2004; Collettini, 2011) including elevated pore fluid pressures, fault weakness controlled by clay-rich gouge materials with low static friction, and rotated (non-Andersonian) principal stress orientations conducive to slip at shallower dips. On the coseismic timescale, dynamically weak fault rocks may govern coseismic fault strength, regardless of their static frictional strength. Laboratory friction experiments on exhumed low-angle normal fault rocks from the Zuccale fault in Italy (Smith & Faulkner, 2010; Niemeijer & Collettini, 2014), the Panamint Valley fault in California (Numelin et al., 2007b) and the Mai'iu fault in Papua New Guinea (Biemiller et al., 2020b) confirm that well-developed gouges in mature LANFs are commonly weak ($\mu_s \leq 0.4$) and velocity-strengthening at shallow subsurface conditions due to the abundance of compliant clay minerals like saponite. Such weak LANFs may not be misoriented for reactivation and slip under Andersonian extensional stresses (e.g., Collettini, 2011; Abers, 2009), whereas stronger faults with Byerlee frictional strength may require favorably rotated principal stresses to slip.

Principal stress orientations near LANFs remain disputed. Early models of LANF formation invoked rotated principal stresses better oriented for shallow slip, with these conditions either persisting throughout the crust or localized near the fault or the brittle-ductile transition (e.g., Spencer & Chase, 1989; Yin, 1989, 1991; Melosh, 1990; Axen, 1992; Wernicke, 1995). Subsequent geodynamic models showed that long-term strain-dependent fault weakening could facilitate flexural rotation of the footwall via a rolling-hinge, a long-term geodynamic mechanism invoked to explain the formation and exhumation of metamorphic core complexes in the back-rotated footwalls of detachment faults. This may explain the protracted mechanical viability of normal faults dipping shallowly in the upper few km of the crust subject to Andersonian extensional loading (Lavier et al., 1999, 2000). Two recent examples highlight the ongoing discourse about different possible stress orientations around LANFs. Structural analysis of the Whipple detachment in the southwest United States (Axen, 2020) suggests that it initiated and slipped as a statically strong ($0.6 \leq \mu_s \leq 0.85$) fault under the influence of local non-Andersonian stresses with a favorably rotated maximum principal stress, σ_1, that plunges ~45° in the dip-direction. In contrast, Mizera et al. (2021) jointly inverted paleostress orientations recorded by calcite twins in the exhumed footwall of the Mai'iu fault along with the orientations of smaller faults in its footwall and hanging wall to infer principal stress orientations in both sections. Their analysis (Figure 1b) found that the hanging wall is characterized by extensional Andersonian stresses with a vertical maximum principal stress and a horizontal minimum principal stress aligned parallel to extension. In the footwall, σ_1 instead appears to be rotated ~15-20° back towards the fault surface, implying that this LANF is even more misoriented for slip in the footwall stress field than it is under standard Andersonian stress conditions.

Mechanical feedback between fault strength and the orientations and amplitudes of tectonic stresses influences not only the long-term structural evolution of fault zones, but also the interseismic, coseismic, and postseismic slip behaviors of active faults. In this study, we develop data-constrained dynamic rupture scenarios to examine how these different tectonic stress conditions affect coseismic rupture characteristics of an active LANF. Recent 3D dynamic rupture models incorporating realistic tectonic stress conditions and complex fault geometries confirm that regional stress orientations are a key factor controlling the dynamic viability of coseismic slip (Palgunadi et al., 2020; Ulrich et al., 2022).

The inherent kinematic asymmetry of normal and reverse dipping faults has been shown to lead to distinct dynamic rupture behaviors, such as reduced or enhanced shallow coseismic slip (Nielsen, 1998; Oglesby et al., 1998, 2000; Aochi, 2018). Aochi (2018) simulated ruptures under extensional and compressional loading conditions constrained by Mohr-Coulomb failure criteria and linear slip-weakening friction. They observed first-order differences in near-surface rupture characteristics between normal and reverse faults. Reduced shallow normal fault slip was attributed to limited shallow shear stress accumulation in these models, resulting from the inherently lower static (Mohr-Coulomb) strength of crustal materials under extension relative to compression. Additionally, dip-angle-dependent shallow clamping or unclamping can occur during normal fault earthquakes due to dynamic stress interactions with the free surface above the shallowest portions of a rupturing normal fault (Nielsen, 1998; Oglesby et al., 1998, 2000).

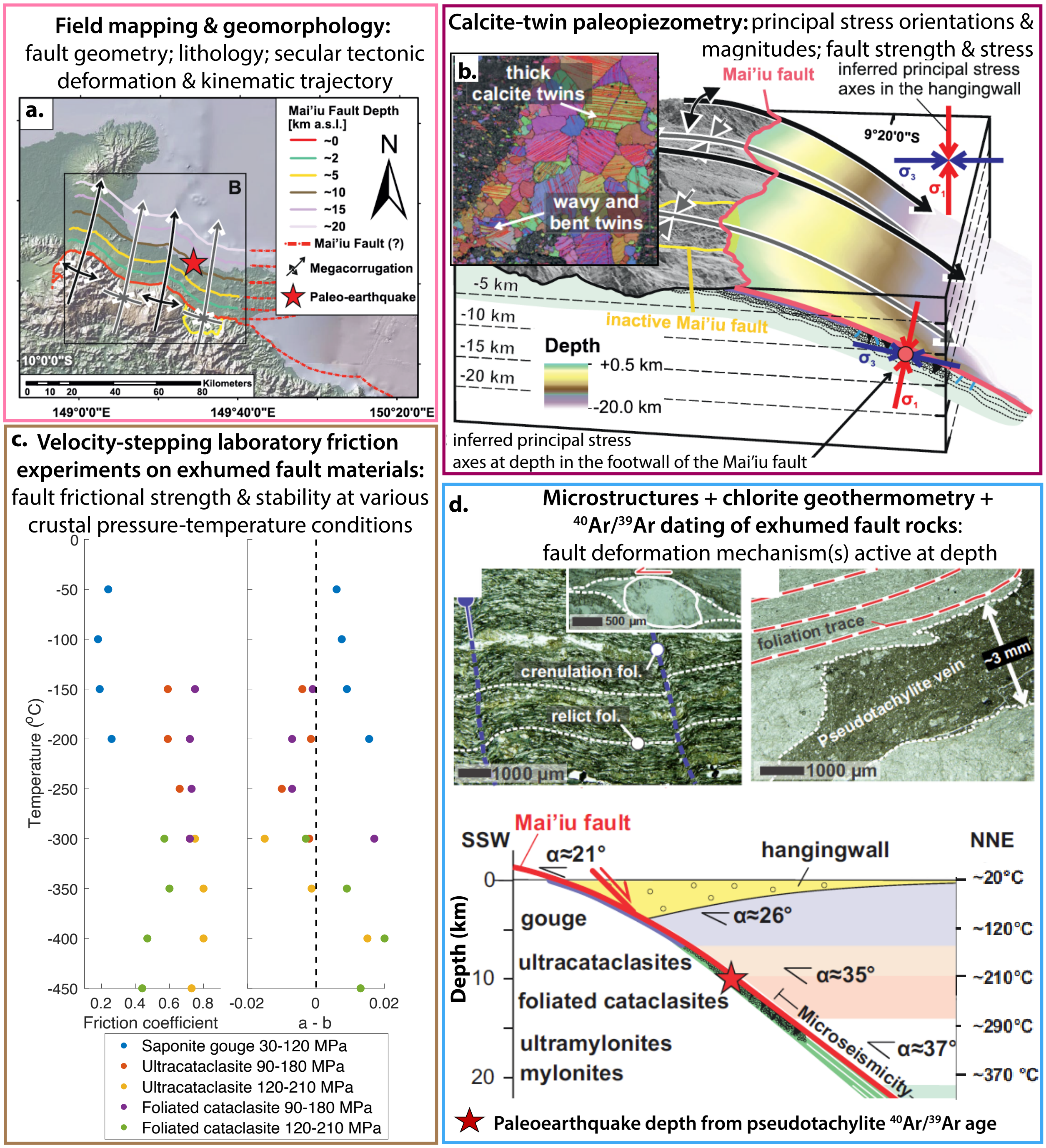

Figure 1. Summary of geologic observations of Mai'iu fault structure, rheology and deformation that can constrain dynamic rupture modeling parameters, initial conditions, or model validation. See references and sections 2.3, 2.4, and 4.1 for more details. Modified from the following references: a.) Mapping confirms shallow dips of 16-24° and geomorphic analysis of fault remnants exhumed atop the corrugated footwall reveals rolling-hinge-style exhumation and ongoing along-strike contraction (Little et al., 2019; Mizera et al., 2019; Webber et al., 2020). b.) Inversion of paleostress orientations recorded by syntectonic calcite veins and minor faults

indicate Andersonian stresses in the hanging wall and back-rotated principal stresses in the footwall (Mizera et al., 2021); paleostresses indicate depth-dependent fault strength including a differential stress peak from ~6-12 km depth (see panel g). c.) Velocity-stepping laboratory friction experiments on exhumed fault materials reveal weak, velocity-strengthening saponitic gouges in the shallow fault zone (<~6 km depth) above stronger, velocity-weakening cataclastic rocks formed and deformed deeper (Biemiller et al., 2020b). d.) Exhumed fault rock microstructures preserve progressive sequence of mixed frictional-viscous deformation including dislocation creep and seismic slip; chlorite geothermometry provides temperature and depth constraints for this deformation sequence (Little et al., 2019; Mizera et al., 2020).

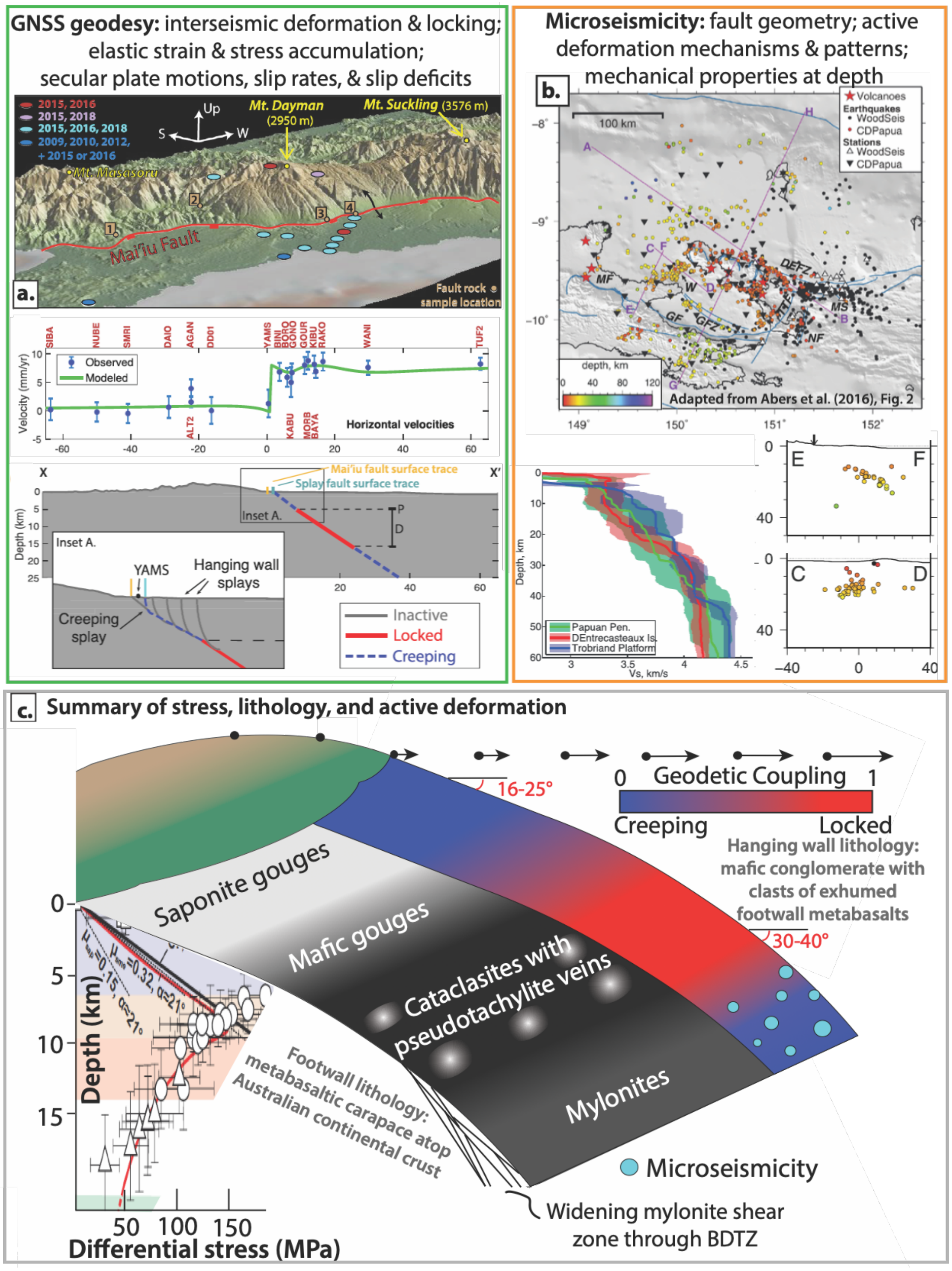

Figure 2. Summary of geophysical and geodetic observations of Mai'iu fault geometry, elastic structure, and active deformation that can constrain dynamic rupture modeling parameters, initial conditions, or model validation. a.) Campaign GNSS measurements across the fault record horizontal extension rates >8 mm/yr and suggest interseismic creep updip and downdip of a strongly locked zone from ~5-13 km depth (Biemiller et al., 2020b). b.) Planar-aligned

microseismicity offshore shows that from ~15-25 km depth the Mai'iu fault dips ~30-40° and deforms by viscous creep accompanied by microseismic brittle failure; seismic velocity modeling constrains depth-dependent temperature, density, and rigidity (Abers et al., 2016; Eilon et al., 2015). c.) Summary figure showing inferred present-day deformation patterns and mechanisms relative to lithological configuration and footwall paleostress profile (Biemiller et al., 2020b; Mizera et al., 2021).

2 Methods

2.1 3D dynamic rupture modeling with SeisSol

Computational scenarios investigating LANF rupture dynamics must account for the curved, shallowly dipping fault geometry and capture free-surface effects. We use SeisSol (www.seissol.org) to solve the nonlinear coupled problem of spontaneous frictional failure and seismic wave propagation. SeisSol uses fully non-uniform, statically adaptive, unstructured tetrahedral meshes enabling geometrically complex models such as curved faults that intersect the Earth's surface. Mesh resolution is adapted to ensure fine sampling of the faults while satisfying the requirements regarding numerical dispersion of pure wave propagation away from the fault (Figures 2a,b). End-to-end computational optimization (Heinecke et al., 2014; Rettenberger et al., 2016; Uphoff et al., 2017), including an efficient local time-stepping algorithm, allows for high efficiency on high-performance computing infrastructure. SeisSol has been verified (Pelties et al., 2014) against a wide range of community benchmarks (Harris et al., 2009, 2011, 2018). SeisSol is freely available (https://github.com/SeisSol/SeisSol).

2.2 Rate-and-state friction with enhanced velocity-weakening

Rate-and-state-dependent friction laws with enhanced velocity weakening allow faults to operate at low average shear stress (e.g., Noda et al., 2009; Dunham et al., 2011). We use a regularized formulation following Dunham et al. (2011) and Harris et al. (2018) as detailed in Supporting Text S1. This formulation introduces severe velocity-weakening in the form of a 1/V behavior of frictional strength which accounts for thermally activated rapid frictional weakening at coseismic slip rates observed in high-velocity laboratory friction experiments, which has been attributed to fault lubrication due to the generation of reaction products, fluidized gouges, or even melts (e.g., Di Toro et al., 2011) and/or flash heating (e.g., Beeler et al., 2008). Note that at slip rates below the weakening velocity V_w, the frictional response to slip-rate variations is governed by the rate-and-state friction parameters *a* and *b*. Materials with a-b>0 are velocity-strengthening, with frictional strength increasing in response to increased slip rate, promoting stable aseismic slip; those with a-b<0 are velocity-weakening and conditionally unstable, with frictional strength decreasing in response to increased slip rate, potentially enabling unstable seismic slip. Friction parameters in our models are described in section 2.3.2 and Figure 4c.

2.3 Data-constrained LANF reference model setup

We develop a LANF reference dynamic rupture model setup, in which we implement physical conditions and mechanical properties inferred from recent observations of southeastern Papua New Guinea and the Mai'iu fault system (Figure 3). These include Andersonian stresses consistent with observationally constrained strike-perpendicular extension and strike-parallel constriction. In subsequent models, we vary parameters such as prestress and fault friction to assess how these conditions affect key dynamic rupture characteristics like the spatial extent and rake of slip, surface uplift, seismic moment, total slip, peak slip rate, rupture speed and stress drop. In this section we describe the reference model parameter choices (Figures 2, 3a; Table 1) along with the field and laboratory evidence on which they are based.

2.3.1 Non-planar fault geometry

Our non-planar fault geometry (Figure 3a,b) is based on that of Webber et al. (2020), who combined surface dip measurements with the microseismic data of Abers et al. (2016) to constrain an interpolated subsurface model of the distinctively corrugated Mai'iu fault. Near the base of the rapidly exhuming Mt. Dayman, the active fault geometry mirrors the concave-down morphology of the domal footwall and exhumed fault surface of Mizera et al. (2019). Along-strike to the southeast, the fault shallows and becomes concave-up beneath the Gwoira rider block, a slice of the original hanging wall captured within the footwall of the active Gwoira splay fault dipping 37-44°. Further southeast, the Mai'iu fault steps offshore where seismic reflection data indicate pervasive normal faulting of its hanging wall basin (Fitz, 2011; Fitz & Mann, 2013a, 2013b), although the lack of surface exposure reduces the accuracy of the fault model here.

Mesh resolution (Figure 3b) is statically adapted to ensure high enough fault resolution (Text S2) and ranges from ~90 m to ~150 m. The full model domain is 1,000 x 1,000 x 500 km^3, much larger than the ~80 x 70 x 40 km^3 region of interest (Figures 2, 4b) to avoid any spurious reflected waves from non-perfect absorbing boundaries. The top boundary is a flat free surface. Automatized unstructured tetrahedral mesh generation is performed with the software PUMGen (https://github.com/SeisSol/PUMGen/), which also exports the mesh into the efficient PUML format used by SeisSol. PUMGen embeds MeshSim from SimMetrix, the underlying mesh generator of SimModeler (www.simmetrix.com), such that the mesh generation may be run in parallel on a compute cluster.

2.3.2 Fault frictional constitutive behaviour

Dramatic frictional weakening (Section 2.2) is the key mechanism governing dynamic (co-seismic) fault weakness in our models. Rate-and-state friction parameters are based on those measured by velocity-stepping laboratory friction experiments performed on various units of the exhumed Mai'iu fault rock sequence under hydrothermal conditions analogous to a range of crustal depths (Biemiller et al., 2020b). Microstructural studies of these fault rocks revealed a sequence of syn-extensionally deformed units progressing from the undeformed metabasaltic protolith to ductilely sheared mylonites to frictional-viscously deformed cataclasites and ultracataclasites to phyllosilicate-rich mafic and saponitic gouges (Little et al., 2019; Mizera et al., 2020). Chlorite geothermometry provides constraints on the temperature and depth ranges over which each fault rock unit deformed and accommodated a major component of fault slip (Mizera et al., 2020). In our models, we map the measured a-b values of each unit to the temperature-depth range over which it is inferred to have deformed (Figure 3c), following the approach of slow slip cycle continuum models (e.g., Liu & Rice, 2007). While our distribution of friction parameters is based directly on laboratory friction experiments coupled with microstructural and geothermometric analyses of the exhumed fault rock sequence, we note that the resulting frictional stability profile mirrors inferred interseismic locking patterns on the Mai'iu fault and thus accords with seismic cycle models that constrain fault friction based on geodetic inferences of interseismic coupling (e.g., Barbot, 2012; Li & Luo, 2021).

In the seismogenic portion of the fault above 15 km, we use a characteristic weakening velocity V_w = 0.1 m/s based on the experimentally observed drop-off of effective friction coefficient from slip rates of 0.01 to 1.0 m/s (Di Toro et al., 2011) and identical to the value of V_w used in SCEC dynamic rupture benchmarks TPV-103, TPV-104, and TPV-105 (Harris et al., 2018). Also, the inferred slip velocity at the onset of severe thermal weakening induced by flash heating is of the order of 0.1 m/s for background temperatures at the middle depth of crustal seismogenic zones (Rice, 2006). While a plausible range of V_w is 0.05 to 2 m/s (Beeler et al., 2008) previous studies explored the effect of variations of V_w (Zheng & Rice, 1998; Nielsen & Carlson, 2000; Ampuero & Ben-Zion, 2008; Gabriel et al., 2012) analytically and numerically identifying predictable effects of tuning the weakening mechanism between dominantly slip-weakening or velocity-weakening behavior. For example, decreasing V_w increases the velocity-weakening rate, and hence reduces the effective nucleation size. Above ~300°C, the exhumed foliated cataclasites and mylonites are primarily velocity-strengthening, and synextensionally formed microstructures indicate that viscous creep mechanisms across a wider and less localized mylonitic shear zone accommodate most offset in this regime. As such, from 15-17.5 km depth the weakening velocity V_w increases from the standard value of 0.1 up to 1.0 (Figure 3d) to enhance the inferred velocity-strengthening behavior at these depths. Additionally, we minimize any dynamic effects of the sharp corners of the fault model geometry from Webber et al. (2020)

by applying a 6-km-wide border of velocity-strengthening material (a-b = 0.006; V_w = 1.0) at the along-strike terminations of the modeled fault (Figure 3a).

Other friction parameters are constant as shown in Figure 3d. The maximum friction coefficient reached during rupture is not a prescribed model parameter. Its value varies along the fault and often exceeds our constant steady-state low-velocity friction coefficient f_0=0.6, but rarely falls below this value. For simplicity, we use an estimated equivalent static friction coefficient $\mu_s \approx f_0 = 0.6$ as a conservative value in the analysis of our simulation results and for constraining prestress magnitudes (see Section 2.4). Our assumed fully weakened friction coefficient, $f_w = 0.2$, is based on the minimum experimentally measured effective friction in the velocity-weakening units of the exhumed Mai'iu fault rock sequence (Biemiller et al., 2020a) and falls within the range of values typically used in dynamic rupture earthquake models that reproduce rupture complexities, such as rupture reactivation and pulse-like ruptures, without assuming small-scale heterogeneities (Noda et al., 2009; Gabriel et al., 2012; Shi & Day, 2013; Palgunadi et al., 2020).

2.3.3. Regional lithological structure

Depth-dependent density (ρ) and elastic moduli (shear modulus G, Lamé parameter λ) (Figure 3e) are derived from the Papuan Peninsula seismic velocity models of Abers et al. (2016) and Eilon et al. (2015) in which V_s ranges from 3.2 km/s at 3 km depth to 4.3 km/s at 60 km depth with associated V_p ranging from 5.8 km/s to 7.7 km/s. Above 3 km these parameters are set to their minimum values of V_s = 3.2 km/s and V_p = 5.8 km/s, more representative of the strong metabasaltic footwall rocks than the weaker sediments in the shallowest hanging wall. Following microstructural analyses that show little evidence of sustained overpressures in the fault core (Little et al., 2019; Mizera et al., 2020), our models use a modest pore fluid pressure ratio, $\lambda_f = P_f/\rho gz$, of 0.66 unless otherwise noted.

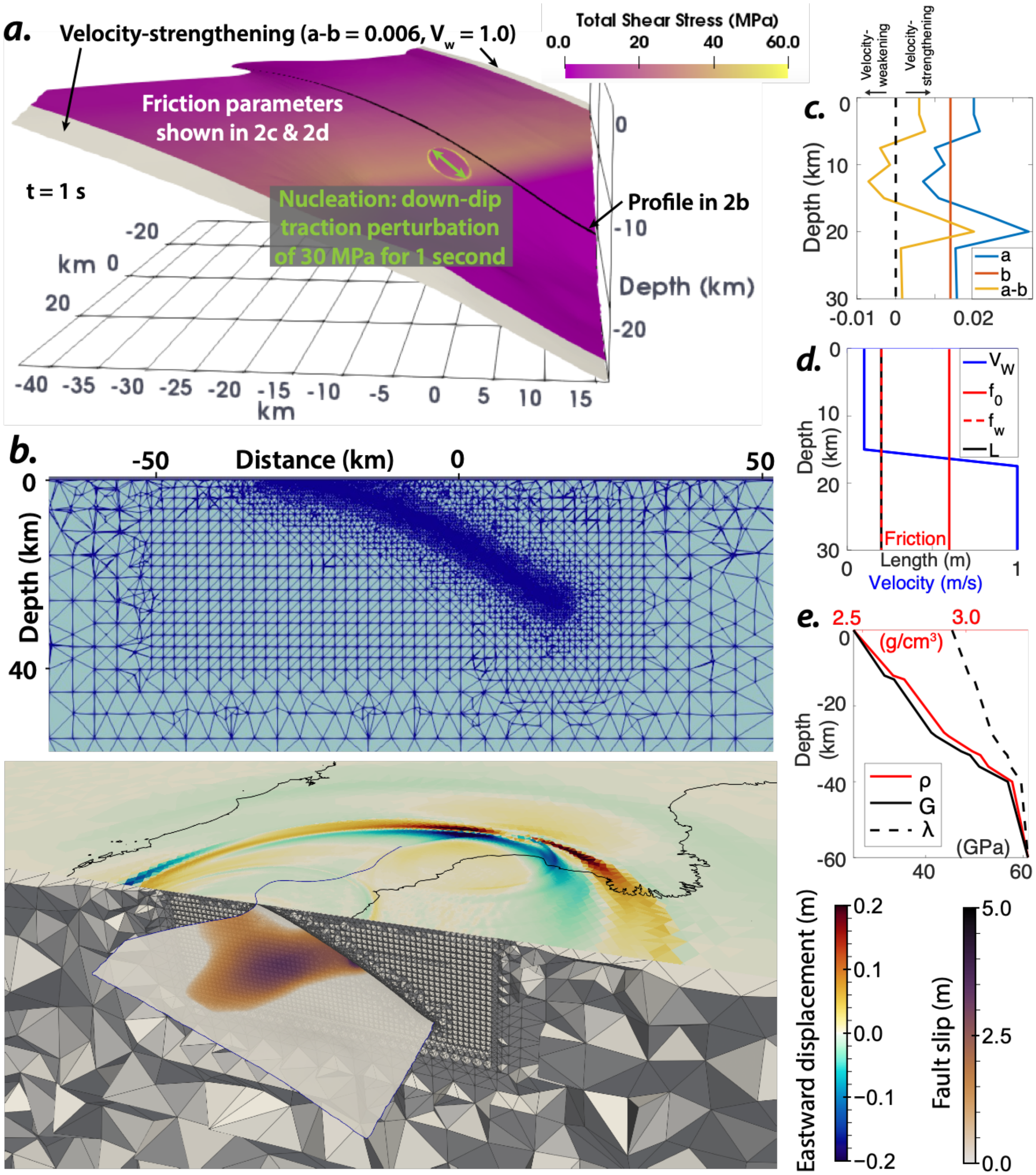

Figure 3. LANF reference dynamic rupture model setup. See sections 2.3-2.5 of the text for details. a.) Shear stress after 1 s in model 1, highlighting the overstressed nucleation zone (green arrows, Section 2.5) and along-strike velocity-strengthening borders (gray). b.) Cross-sections of SeisSol's unstructured tetrahedral computational mesh showing representative near-fault refinement. c-d.) Depth-dependence of fast-velocity weakening rate-and-state friction parameters. e.) Depth-dependence of density and elastic moduli.

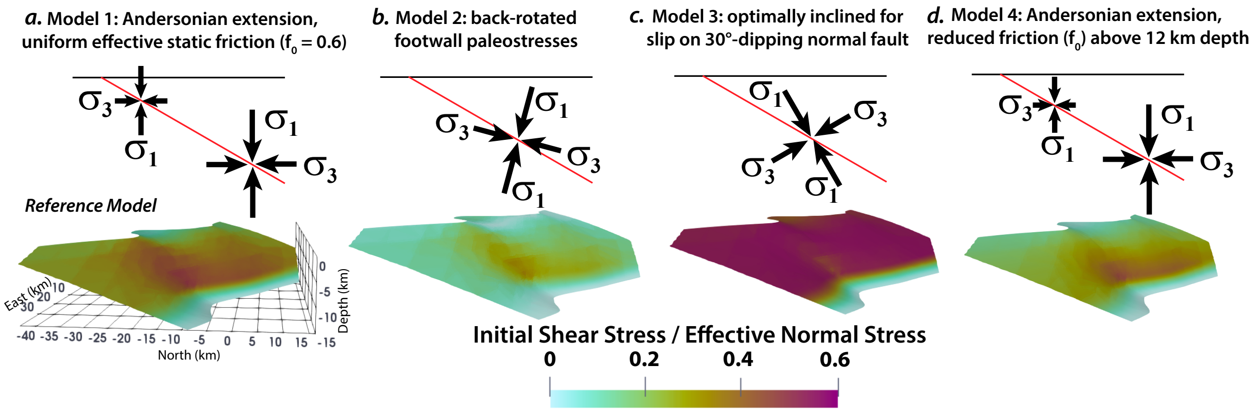

Figure 4. a-d.) Schematic of principal stress orientations (above) and ratios of initial shear to effective normal stress, reflecting slip tendency (below) in models 1-4, respectively. We can consider f_0 as an estimate of the static friction coefficient (see Sections 2.3.2 and 2.4). Thus, the fault is initially close to failure when its apparent strength (initial shear over effective normal stress) is close to ~0.6 (except in model 4 at shallow depth, where a reduced f_0 is assumed in the computation of initial fault stress).

Model #	Figure #	T_{nuc}	r_{nuc}	R_0	λ_f	f_0	Stress	Plunge of σ_1	Plunge direction of σ_1	M_w	Fault geometry
		(MPa)	(km)				Andersonian extension with constant f_0, unless noted	(°)			Webber et al. (2020) unless noted
1	3, 4	30	2	0.95	0.66	0.6		90		7.14	
2	4	45	3	0.95	0.66	0.6	Footwall paleostresses: backwards-inclined σ_1	15	S30°W	6.42	
3	4	30	2	0.95	0.66	0.6	Inclined σ_1 well-oriented for LANF slip	30	N30°E	7.79	
4	4	30	2	0.95	0.66	0.2-0.6	Andersonian extension with depth-varying f_0	90		6.88	

Table 1. Parameters varied in dynamic rupture simulation scenarios: maximum magnitude of nucleation overstress T_{nuc}, nucleation radius r_{nuc}, initial prestress ratio R_0 (equation 1), pore fluid pressure ratio λ_f (section 2.3.3), effective static friction f_0, and resulting earthquake magnitude M_w.

2.4 Regional stress constraints and LANF loading

We simulate ruptures under different prestress conditions (Table 1) including Andersonian extension (Figure 4a,d) and stress fields where the maximum principal stress is non-vertical and plunges towards or away from the dip-slip direction (Figure 4b,c). Paleostress inversions (Mizera et al., 2021) and ongoing folding of the megacorrugated footwall (Little et al., 2019; Webber et al., 2020) indicate that strike-perpendicular extension is accompanied by strike-parallel constriction. The reference model, model 1 (Figure 4a, Table 1), employs an Andersonian stress field with the intermediate principal stress σ_2 oriented along-strike (N60W) resulting in the minimum principal stress σ_3 aligned parallel to the extension direction (N30E). The relative magnitudes of the principal stresses can be quantified by the stress-shape ratio, $\Phi = \frac{\sigma_2-\sigma_3}{\sigma_1-\sigma_3}$, where Φ ranges from 0 (uniaxial compression with $\sigma_1 >> \sigma_2 \approx \sigma_3$) to 1 (axial constriction with $\sigma_1 \approx \sigma_2 >> \sigma_3$). Following Mizera et al. (2021) who report strongly constrictional stresses, we assume $\Phi = 0.8$ in all models.

How close any patch on the fault is to failure can be expressed by its apparent strength, the closeness of the ratio of initial shear stress over effective normal stress to an estimated equivalent static friction coefficient $\mu_s \approx f_0 = 0.6$ (Fig. 3) following Mohr-Coulomb theory. This apparent strength of the fault can be related to dynamic parameters which constrain the magnitude of deviatoric stresses (Ulrich et al., 2019b). We define the relative prestress ratio, R (Aochi & Madariaga, 2003), which is the ratio of the potential stress drop, $\Delta\tau$, to the full breakdown strength drop, $\Delta\tau_b$:

$$R = \frac{\Delta\tau}{\Delta\tau_b} = \frac{\tau_0-\mu_d\sigma_n'}{(\mu_s-\mu_d)\sigma_n'} \approx \frac{\tau_0-f_w\sigma_n'}{(f_0-f_w)\sigma_n'} \qquad (1)$$

where τ_0 is the initial shear stress, σ_n' is the initial effective normal stress, $\mu_s \approx f_0$ is the estimated equivalent static friction coefficient and $\mu_d \approx f_w$ is the estimated equivalent dynamic friction coefficient. To compute R we assume $\mu_d = f_w = 0.2$, as we observe that fully weakened friction is typically reached. R is a relative fault strength defined with respect to the frictional strength drop. We prescribe only the maximum prestress ratio, R_0, which is the prestress ratio of an optimally oriented fault in the stress field. Local fault orientation controls the initial prestress at any point on the fault, with $R \leq R_0$. For $R = R_0$, the fault segment is optimally oriented with respect to the local stress conditions. For $R_0 = 1$ an optimally oriented fault segment is also critically stressed.

Stress magnitudes for each simulation are computed using observations following the approach of Ulrich et al. (2019b) assuming normal-sense dip-slip based on Φ, λ_f, R_0, the azimuth of σ_2, and the frictional strength of the fault given by f_0. In Models 1-4, $R_0 = 0.95$, $\lambda_f = 0.66$, $\Phi = 0.8$, and σ_2 strikes N60W. Model variants with lower R_0 and λ_f (Figures S1, S2) require larger nucleation overstresses to rupture past the nucleation zone, but generally exhibit slip patterns similar to the reference model, highlighting the prevalence of these rupture characteristics over a wide range of initial conditions. We apply a smooth depth-dependent deviatoric stress taper to account for viscous creep below the brittle-ductile transition zone that limits the accumulation of elastic strains and deviatoric stresses around deeper portions of the shear zone during the interseismic period. We apply this taper from 11-15 km depth based on diffusion creep and grain-boundary sliding recorded microstructurally in the fault rocks deformed below the paleopiezometrically determined fault strength peak from 6-12 km depth (Mizera et al., 2020, 2021).

2.5 Earthquake nucleation

Earthquakes in dynamic rupture models can be nucleated in a variety of ways. We aim for the nucleation procedure that requires the smallest perturbation in order to minimize artificial effects of the nucleation conditions on rupture behavior (e.g., Galis et al., 2015). We nucleate slip at a reasonable location on the fault based on available data. Nucleation is commonly imposed through a temporary local reduction of fault frictional strength (e.g., Harris et al., 2021), or via temporary local increased stresses (e.g., Galis et al., 2015). Here, we impose a temporary increase in the down-dip shear traction on the fault (T_{nuc}) that evolves smoothly in both space and time over a spherical region of radius r_{nuc} and a nucleation duration t_{nuc} (Figure S9). We assume earthquakes on the Mai'iu fault are most likely to nucleate in the strong velocity-weakening cataclastic fault rocks in the vicinity of the paleopiezometric stress and strength peak and the geodetically locked zone, around 10-12 km depth. Thus, we apply the nucleation conditions in a central location along-strike centered at a depth of 11 km. Through trial-and-error, we derive the smallest possible shear traction perturbation that leads to rupture propagation in most models, using T_{nuc} of 30 MPa, r_{nuc} of 2 km, and t_{nuc} of 1 second.

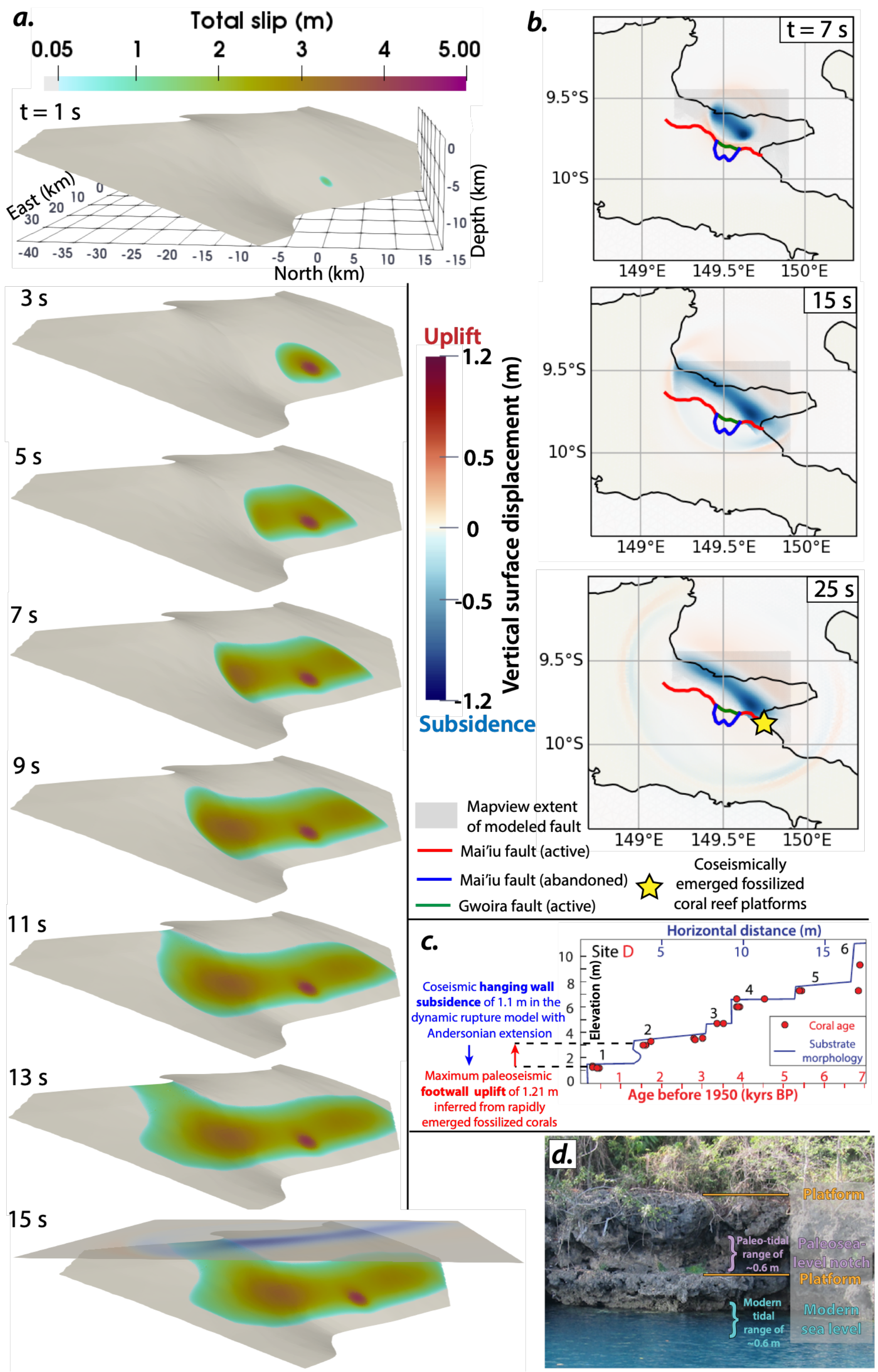

Figure 5. Temporal evolution of a.) fault slip and b.) vertical surface displacement in the reference model. The last snapshot at 15s simulation time in a) includes a perspective view of the accumulated vertical surface displacement. The gray shaded rectangular area in b) is the mapview area of our full modeled fault geometry (full fault model domain shown in Figure 3a). c.) Magnitudes of modeled coseismic hanging-wall subsidence of ~1 m (blue arrow) beneath Goodenough Bay are similar to maximum paleoseismic displacements (red arrow) inferred from

episodically emerged fossilized coral platforms found there, as shown by the elevations and U/Th ages of d.) sampled platforms from Western Goodenough Bay (from Biemiller et al., 2020a).

3. Results

In the following sections we describe four key LANF dynamic rupture models including one preferred reference model. In the Supporting Information we detail additional results from dynamic rupture simulations probing model sensitivity, including models with alternate pre-stresses that are initially farther from failure, models with alternate pore fluid pressures, variants of model 3 with stronger imposed nucleation conditions, models with planar detachment fault geometries, models without velocity-strengthening materials in the shallow parts of the fault, models with different nucleation locations, and models with different characteristic weakening velocities V_w (Table S1, Figures S1-S8).

3.1 Reference model based on inferred hanging-wall stresses: Andersonian extension and uniform fault static friction f_0= 0.6

Figures 4a and 4b show the evolution of fault slip and vertical surface displacement over 15 s of the simulated M_w 7.1 earthquake in the reference model. Figures 5a-d summarize accumulated fault slip, rupture velocity, total shear stress and stress drop which we estimate as the difference between the initial (at t=0 s) and final total shear stress after 15 seconds simulation time.Model 1 is loaded with Andersonian extensional stresses, as inferred from paleostress analysis of hanging-wall faults (Mizera et al., 2021), computed for Byerlee frictional fault strength assuming uniform f_0= 0.6 (Figure 4a; Table 1). The imposed nucleation traction perturbation lasts one second, and subsequent rupture is spontaneous and self-sustained. Rupture initially propagates updip towards the surface and in both directions along-strike, but arrests downdip near the deviatoric stress taper and the transition to velocity-strengthening fault materials. In the western portion of the fault downdip of Mt. Dayman, updip rupture propagation is arrested at around 5 km depth, near the transition to shallow velocity-strengthening gouges. In contrast, rupture penetrates the shallow velocity-strengthening portion of the eastern segment along Goodenough Bay resulting in 1-2 m of slip at the surface. Lateral rupture propagation proceeds along-strike in both directions within the velocity-weakening units between 5-13 km depth until reaching the edges of the modeled fault, where imposed velocity-strengthening borders arrest rupture. Rupture propagates at 3-4 km/s rupture velocity on most of the slipped fault (Figure 6b), but briefly reaches supershear speeds approaching the assumed respective local P-wave velocities ranging from 6.3 km/s close to the hypocentre to 5.8 km/s near the free surface. Supershear rupture remains localized within ~1 km of the nucleation zone and in a small patch of the shallow Goodenough segment, where unsustained supershear slip initiates slightly ahead of the main rupture front. This shallow supershear rupture behavior arises following the emergence of a secondary rupture front updip of the initially slipping patch in dynamic rupture models of more steeply dipping normal faults with a free surface, which Oglesby et al. (1998) attribute to a temporary reduction of normal stress updip of the initially slipped portion that brings the shallow portion of the fault near the free surface close to failure before the initial rupture front reaches it. Free surface interactions promoting shallow supershear rupture (Kaneko & Lapusta, 2010) and transient local stress perturbations from trapped waves in the hanging wall (e.g., Oglesby et al., 1998; Huang et al., 2012) likely amplify the fast rupture velocities associated with this 'rupture jumping ahead' behavior. Although shallow updip rupture jumping appears mechanically feasible, we are not aware of any well-documented instances of supershear rupture during LANF earthquakes. Between 6-13 km depth, stress drops range from 4-11 MPa (Figure 6d), while in the shallow slipped portion stress drops are limited to <3 MPa, which is a consequence of the linear depth-dependence of the initial loading.

Coseismic vertical surface displacements are punctuated by dynamic along-strike and counter-dip-direction propagation of a surface-wave-mediated uplift front, 30-40 cm high, that initiates atop the hanging wall, followed closely by along-strike propagation of a more pronounced pattern of subsidence in the hanging wall which outlines the final static displacement pattern of hanging wall subsidence of up to 1.1 m. Static footwall uplift occurs only at the trace of the Goodenough segment and is limited to < 3 cm. With observationally constrained mechanical properties and fault geometry subject to stresses consistent with structurally inferred hanging-wall stresses, this model generates coseismic vertical surface displacements in western Goodenough Bay similar to paleoseismic offsets inferred from rapidly emerged fossilized coral platforms there (Figure 5b-d; see section 4.1 for details). Thus, Model 1 is a compelling and appropriate reference model against which to compare results from other rupture scenarios.

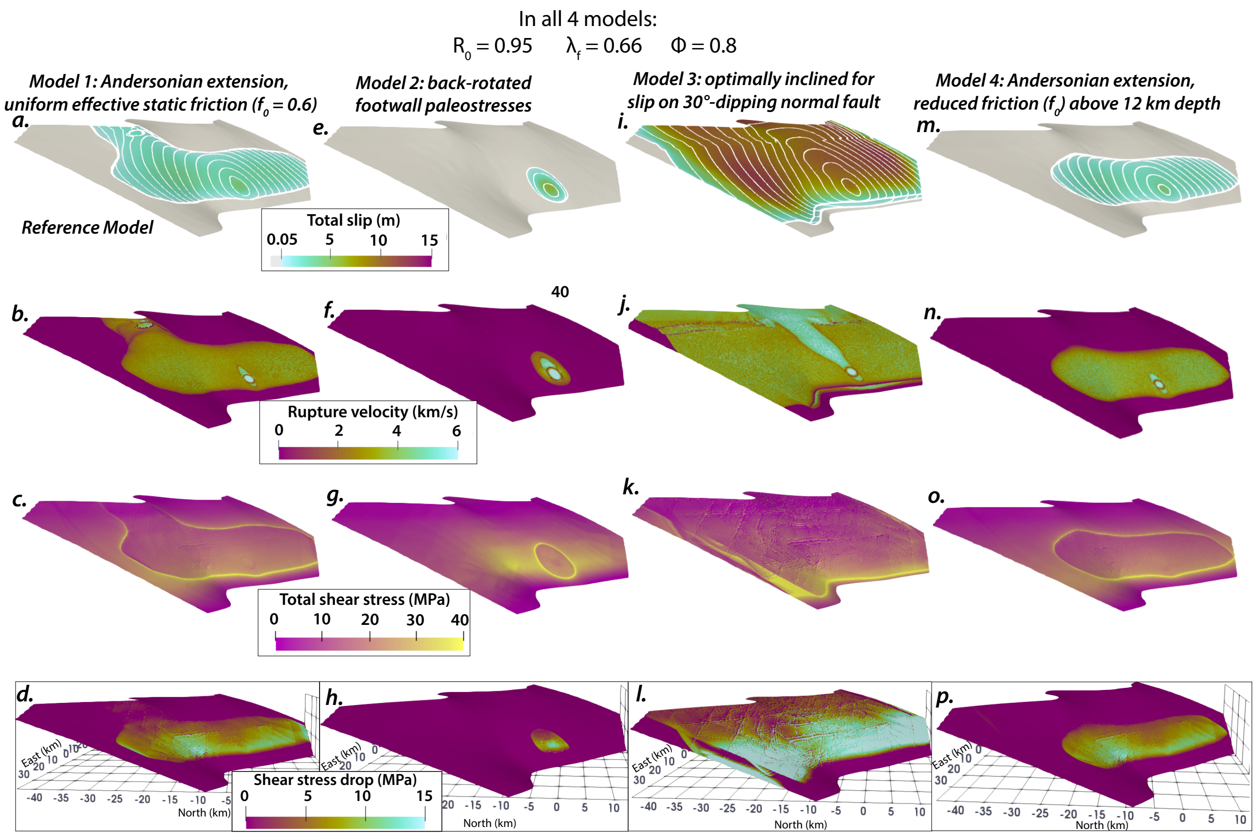

Figure 6. Results after 15 seconds for models 1 (a-d), 2 (e-h), 3 (i-l) and 4 (m-p). Top row: Total slip (m) with white rupture contours plotted every 1 s. Second row: Rupture velocity (km/s). Localized supershear rupture episodes appear as light blue, e.g. updip of the nucleation zone in model 3. Third row: Postseismic shear stress. Shallow stress concentrations updip of a buried rupture patch (c,o) may promote shallow afterslip or interseismic creep (see Discussion). Bottom row: modelled stress drop (MPa) estimated as the change in total shear stress from t=0s to t=15s.

3.2 Model 2: inclined principal stress orientations inferred from syntectonic calcite veins in the exhumed footwall

The setup of Model 2 is identical to the reference model except that initial stresses are calculated based on a σ_1 orientation plunging 15° SSW, now consistent with the paleopiezometrically inferred footwall stress orientations (Mizera et al., 2021) and optimally oriented for dip-slip on a normal fault dipping 75°. With such backwards-inclined principal stresses, LANFs should be even less well-aligned for slip than they are under Andersonian conditions, as illustrated by the decreased ratio of initial shear stress over initial effective normal stress (Figure 4b). With identical imposed nucleation tractions to those that generate a M_w 7.1 event in the reference model, rupture fails to nucleate under these rotated principal stress conditions and slip remains limited to the predefined nucleation patch. Increasing the magnitude and area of the imposed overstress results in more slip in and around the nucleation zone, but does not lead to a dynamically viable model with rupture propagating onto other parts of the fault (Figure S3). For example, the panels in Figure 6 associated with model 2 result from a model with 50% increased nucleation conditions (T_{nuc} = 45 MPa, r_{nuc} = 3 km), yet slip remains limited to within a few km of the nucleation zone. R_0 is already close to 1 in models 1-4 and cannot be increased further to enhance slip tendency and promote unstable slip. Thus, these backwards-inclined principal stress orientations appear to be incompatible with any dynamically viable rupture scenarios.

3.3 Model 3: inclined principal stress orientations aligned optimally for dip-slip on a normal fault dipping 30°

Many models for LANF formation propose that rotated principal stress orientations through part or all of the crust establish a stress field conducive to normal-sense slip on shallowly-dipping faults, with σ_1 plunging at a small angle to the detachment (e.g., Spencer & Chase, 1989; Lister & Davis, 1989; Yin, 1989; Melosh, 1990). We test the dynamic effects of such a stress field in model 3. Conditions in model 3 are identical to model 2 except that σ_1 plunges 30° in the opposite direction (NNE), such that it is more closely aligned with the dipping fault. Such rotated stresses should be optimally aligned for normal-sense slip on a fault dipping 30°, as highlighted by the increased ratio of initial shear stress over initial effective normal stress (Figure 4c). As in the reference model, rupture in model 3 initially propagates rapidly in all directions except down-dip (Figure 6i); however, it subsequently accelerates updip rather than arresting near the transition to velocity-strengthening material. After 7 s, slip penetrates to the surface on the most shallowly-dipping segment beneath the Gwoira rider block. Subsequent rupture propagates in both directions along-strike at all depths above ~14 km, saturating the entire fault with slip and even rupturing into the strongly velocity-strengthening barriers at the along-strike edges of the model. This M_w 7.8 earthquake results in maximum slip of more than 12 m, including up to 11 m of slip at the surface. Unlike the reference model, this event includes localized but significant supershear rupture episodes directly updip of the nucleation zone (Figure 6j). Modelled stress drops are larger than in Model 1, ranging from 15 MPa to more than 20 MPa between 6 and 13 km depth (Figure 6l).

3.4 Model 4: Andersonian extensional stresses adjusted for reduced near-surface static effective friction ($0.25 \leq f_0 \leq 0.6$)

Finally, Model 4 considers decreased near-surface fault stress and strength conditions implemented through reduced effective static friction f_0 above 12 km depth. Mechanical models of LANF formation commonly invoke significant shallow fault weakening to explain how these normal faults penetrate through the upper crust and remain active at such shallow dips (e.g., Axen, 1992; Collettini, 2011). In addition, geodynamic models that develop LANFs via footwall rotation through a self-consistent rolling-hinge typically require finite strain-weakening mechanisms. These reduce fault strength with continued slip and flexural rotation of the fault and exhuming footwall, leading to very low effective fault strength near the surface (e.g., Buck, 1988; Lavier et al., 1999, 2000; Whitney et al., 2013). Possible brittle strain-weakening mechanisms include loss of cohesion and precipitation of weak clay minerals during prolonged slip, while viscous strain-weakening may occur via grain-size reduction and related strain localization. Thus, it appears feasible that crustal stresses near such weak faults may be modulated by local fault strength (Axen, 1992; Rice, 1992) and vary with depth based on fault rock and gouge composition. In model 4, Andersonian extensional stresses are computed as in the reference model, but assuming that the shallow equivalent static friction coefficient f_0 decreases linearly from 0.6 at 12 km depth to 0.25 at the surface following experimentally measured friction coefficients of the exhumed Mai'iu fault rocks (Biemiller et al., 2020b). The resulting earthquake mirrors most of the slip behavior of the reference model, but rupture notably does not penetrate to the surface through the shallow velocity-strengthening region of any fault segment. Instead, slip is limited to depths of ~6-13 km within a slightly narrower along-strike region, resulting in less total slip everywhere during this smaller M_w 7.0 event.

4. Discussion

4.1 Integration of observations to constrain dynamic rupture modeling of LANF earthquake scenarios

Initial conditions of dynamic rupture modeling include the preexisting state of stress and the frictional properties governing fault strength and sliding, as well as the lithological structure and fault geometries. We demonstrate how to integrate geophysical and geologic observations to constrain all required initial conditions for realistic LANF earthquake scenarios. For example, we impose a linearly decreasing deviatoric stress ramp from 11-15 km depth based on the paleostress depth profile of Mizera et al. (2021), which successfully limits the downdip rupture extent in all models to between 13-15 km depth, in line with both the geodetically inferred downdip edge of interseismic locking and the updip extent of planar-aligned microseismicity inferred to delineate the viscously creeping mylonitic shear zone. Our modelled earthquakes agree with realistic levels of static and dynamic frictional resistance, slip, rupture speed and stress drop and adopt a friction law with severe velocity weakening that enables complex rupture and realistic amounts of slip, in contrast to simplified friction laws. Our models do not explain unique features of a particular instrumentally recorded earthquake. Instead, we develop a suite of data-constrained dynamic rupture simulations to probe longer-term tectonic and geomechanical questions, such as 'what is the state of stress around active LANFs?' (sections 4.3 & 4.4). While this distinction is partially necessitated by the absence of sufficiently well-documented modern

LANF earthquakes, our approach highlights how dynamic rupture models can be used to address interdisciplinary and multi-timescale geoscience problems, augmenting the typical scope of observational seismology. In addition, we extend recent studies that leverage data-constrained dynamic rupture scenarios to better understand the future rupture behavior of active seismogenic faults that have not slipped in a large earthquake during the modern instrumental record, but nonetheless pose significant hazards to nearby communities (Aochi & Ulrich, 2015; Ramos & Huang, 2019; Ramos et al., 2021; Aslam et al., 2021; Melgar, 2021) for the first time to a LANF setting.

4.2 Implications of the reference model for the seismic cycle and hazard potential of the Mai'iu fault

Geologic and geophysical evidence of past and ongoing Mai'iu fault deformation align well with areas of the fault that dynamically slip in the reference model with strike-perpendicular Andersonian extension in a constrictional stress field, modest pore fluid pressure, and high closeness-to-failure for well-oriented fault segments. Although the same depth-dependent frictional and mechanical properties are assumed uniformly along strike, rupture propagates to the surface on the eastern Goodenough segment, but not on the central Gwoira segment, where the capture and transport of the overlying Gwoira rider block indicates abandonment of the shallowest portion of the Mai'iu fault (Little et al., 2019; Webber et al., 2020). We attribute these preferential shallow rupture patterns to static and dynamic effects associated with the local fault geometry: the Goodenough segment dips more steeply near the surface than the Gwoira or Dayman segments. In terms of static fault mechanical viability, the more steeply-dipping segments are better-oriented for normal slip. Co-seismically, rupture asymmetry and static and dynamic stress interactions between a slipping normal fault and the free surface can either hinder or promote near-surface rupture depending on the fault dip (Nielsen, 1998, Oglesby et al., 1998, 2000, 2008; Ma and Beroza, 2008).

Additional dynamic increase of shallow shear stresses close to the free-surface is caused by trapped waves between the free-surface and the hanging-wall favoring shallow slip (e.g., Oglesby et al., 1998; Huang et al., 2012). These combined static and dynamic effects promote shallow rupture by dynamically weakening normal faults dipping 30°-75° but impede shallow rupture on those dipping less than 30° or more than 75° (Oglesby et al., 1998). This effect of fault dip on dynamic rupture viability is highlighted and isolated in alternative models with planar detachments dipping 25° and 35° (Figure S4): rupture fails to propagate more than a few km past the nucleation zone on the 25°-dipping fault, whereas the entire 35°-dipping fault slips above ~12 km depth with rupture propagating to the surface everywhere.

Rupture on the Gwoira and Dayman segments notably arrests around 5 km depth, at the updip edge of the geodetically inferred locked zone. This modeled rupture pattern raises the interesting possibility that postseismic stress concentrations leftover from an earthquake may drive shallow afterslip and/or interseismic creep updip of the area that slipped coseismically, within the weak velocity-strengthening saponitic gouges found there. Figure 6 (third row) illustrates modeled postseismic shear stress concentrations outlining the rupture areas, which in Models 1 and 4 include large shear stress increases updip of the buried rupture patch that could drive shallow afterslip or interseismic creep (Figure 6c,o). Additionally, shallower slip on all segments in an alternate model with a-b<0 above 15 km depth confirms the important stabilizing role of the shallow velocity-strengthening gouges in limiting shallow coseismic slip (Figure S5).

Distinct platform-notch-platform sequences of fossilized coral reefs along the southwestern Goodenough Bay shoreline indicate punctuated emergence events with average maximum vertical displacements of 1.3 m (Figure 5c,d; Biemiller et al., 2020a). Rupture in the reference model propagates to the surface on the segment directly below these emerged corals, resulting in ~2 m of near-surface slip and static vertical coseismic offsets of up to 1.1 m (Figure 5). Interestingly, the modeled offsets consist almost entirely of hanging-wall subsidence with only a few cm of footwall uplift. Based on the faceted coastal morphology and presence of older fossilized corals at >300 m elevation (Mann & Taylor, 2002; Mann et al., 2004, 2009), these younger emerged coral platforms were previously interpreted as products of coseismic footwall uplift during normal fault earthquakes (Biemiller et al., 2020a); however, our dynamic rupture models suggest that these platform-notch sequences may form due to abrupt coseismic hanging wall subsidence but emerge during more gradual footwall uplift that persists through most or all of the seismic cycle. This process is more consistent with geodetically observed coseismic vertical displacements from continental normal fault earthquakes, which typically show pronounced hanging wall subsidence and minor-to-moderate footwall uplift (e.g., Stein & Barrientos, 1985; Cheloni et al., 2017). Additionally, gradual emergence may explain the poor along-strike preservation of these pronounced platforms: only the largest platforms on the most rapidly uplifting parts of the coastline can survive the intense erosion they experience during gradual emergence through the intertidal zone.

4.3 Stress orientations near seismogenic detachment faults

Detachment faults commonly juxtapose strong metamorphic footwall rocks against weaker sedimentary rocks in the hanging wall (e.g., Whitney et al., 2013), but the effect of such strength contrasts on the interseismic loading of these faults remains unclear. Dynamic rupture models of planar bimaterial normal faults show that peak ground motions are larger when the hanging wall contains more compliant material, but that this strength configuration reduces the coseismic strength drop on the shallow part of the fault (Ma & Beroza, 2008). Failed nucleation in Model 2 implies that applied stresses on the Mai'iu fault are more similar to those in its hanging wall than its footwall, suggesting that effective stress on the seismogenic portions of detachments may be limited by the strength of the hanging wall, which is typically lower than that of the metamorphic footwall due to the presence of weaker, less consolidated, unmetamorphosed sedimentary rocks. Additionally, stresses in the footwall and hanging wall may be largely decoupled if the detachment is weak, as suggested by paleopiezometry and geodynamic models of the Mai'iu fault (Biemiller et al., 2019; Mizera et al., 2021), not unlike local stress orientation heterogeneities observed in the shallow subduction margins of Nankai (Lin et al., 2016) and Hikurangi (McNamara et al., 2021) which may be tied to effective stress and pore pressure discontinuities across the weak, impermeable shallow subduction interface fault zones (e.g., Skarbek & Saffer, 2009).

Although rotated principal stresses better-aligned for low-angle normal-sense slip have been proposed for some LANFs, we find that these conditions are not necessary to explain continued slip on these faults, as highlighted by recent fault reactivation analyses (e.g., Abers, 2009; Collettini, 2011). If any detachment faults formed and remain active within optimally inclined stress fields, these are certainly the most likely to host large (M_w >8) damaging earthquakes (Figure 6i); however, these stress conditions do not appear to be common or representative of most extensional settings. Our dynamic rupture scenario with well-aligned principal stresses features high stress drops (>15 MPa; Figure 6l) and supershear rupture velocities (larger than the seismic shear wave velocity; Figure 6j). Sustained supershear rupture transition is associated with larger relative prestress ratio R_0 (e.g., Andrews, 1976; Das & Aki, 1977; Dunham et al., 2007; Gabriel et al., 2012). The expected stress drop in our models can be estimated to first order as $(1-\lambda_f)\sigma_n'(\mu_s-\mu_d)R_0$ (Ulrich et al., 2019b) which in model 4, for example, increases from 0 MPa at the surface to 24 MPa at 15 km depth. Thus, both the dynamically modeled stress drop and the rupture velocity could be decreased in models with lower R_0; however, low R_0 would hinder rupture nucleation on any segment and would imply that even well-oriented parts of the fault are stressed far from criticality, which is at odds with observations from continental drilling (e.g., Townend & Zoback, 2000; Zoback & Townend, 2001) and post-glacial fault reactivation (e.g., Steffen & Steffen, 2021) that indicate the crust is critically stressed (e.g., Zoback & Zoback, 2007). Sibson (1990) distinguished two classes of misoriented faults: those that are *unfavorably oriented* under Anderson-Byerlee conditions, and those that are *severely misoriented* and require pore fluid pressures to exceed σ_3 for the fault to remain mechanically viable, breaching the so-called 'hydrofrac limit' (e.g., Abers, 2009) at which deformation proceeds via the opening of new hydrofractures rather than continued fault slip. Although the most shallowly dipping portions of LANFs appear *unfavorably oriented* to Andersonian stresses, their local static frictional weakness may keep them from being severely misoriented for long-term slip viability by reducing the lock-up angle of their hydrofrac limit (e.g., Collettini, 2011), enabling dynamic slip viability during ruptures nucleated on nearby segments that may be better-oriented. In the case of the Mai'iu fault, steeper dips of 30-40° at seismogenic depths of 12-15 km indicate the fault is better-oriented at depth and help explain the mechanical viability of rupture nucleation on this fault.

4.4 LANF stress criticality and implications for 'keystone' faults and complex ruptures

Understanding whether LANFs must be critically stressed to slip coseismically could help assess whether LANF segments control the interseismic strength and eventual seismic failure of multi-fault detachment systems. Our dynamic rupture modeling explains how coseismic slip can penetrate into unexpected parts of faults that do not appear well-primed for seismic slip, like segments poorly-oriented relative to the regional stress field, areas with velocity-strengthening behavior, and portions not initially stressed close to static frictional failure. We note that Models 1-4 all include R_0=0.95, meaning that regardless of the given stress orientation scenario, any fault segment well-oriented for slip in their respective stress field is initially stressed close to failure. Under Andersonian extension, for example, more steeply-dipping normal faults are expected to be stressed to failure and rupture coseismically before their shallowly dipping counterparts. However, recent evidence from an active multi-fault detachment system in Baja California suggests well-oriented faults near a low-angle detachment may be stressed to failure without rupturing seismically until the underlying detachment is critically stressed (Fletcher et al., 2016).

For the best-documented modern earthquake involving possible LANF slip, the 2010 M_w 7.2 El-Mayor Cucapah event, Fletcher et al. (2016) proposed that the LANF segment acted interseismically as the keystone fault, limiting seismic slip on an intersecting network of better-oriented critically-stressed faults until eventually the poorly-oriented detachment was critically stressed to failure. Model 3 with nearly critically-stressed conditions in the hypocentral region generates our largest modeled earthquake and presents unusually large stress drops and supershear rupture velocities, while our reference model is initially subcritically stressed at hypocentral depths but generates coseismic surface displacements similar to those recorded paleoseismically. Thus, our results suggest that LANFs can slip coseismically without being interseismically critically stressed near their static frictional failure strength. Nonetheless, similar to the keystone fault model, classically better-oriented detachment segments and neighboring normal faults would be stressed closer to failure than the shallowly-dipping parts of the Mai'iu fault in the Andersonian extensional stress field of the reference model.

Our models suggest that LANFs are dynamically viable under common crustal loading conditions, yet they do not fully resolve the perplexing scarcity of large earthquakes with well-resolved low-angle normal-sense focal mechanisms in the modern instrumental record (Jackson & White, 1989; Collettini & Sibson, 2001), for which various mechanical explanations have been proposed. Wernicke (1995) posited that LANF earthquakes are particularly rare because these faults typically accommodate relatively slow extension rates (a few mm/yr) and thus host only infrequent earthquakes; however, faster extension rates ≥ 1 cm/yr across the Mai'iu fault (Wallace et al., 2014; Webber et al., 2018; Biemiller et al., 2020b) and the Banda detachment (Cummins et al., 2020) suggest these LANFs should host more frequent earthquakes. Nonetheless, paleoseismically recorded recurrence intervals from the Goodenough portion of the Mai'iu fault range from 482 – 1590 years (Biemiller et al., 2020a). It is plausible that large LANF earthquakes have not been recorded simply because their recurrence intervals are much longer than the relatively short instrumental record. Building on the keystone fault model of Fletcher et al. (2016), Karlsson (2021) proposed that if LANFs typically slip in complex multi-fault ruptures that involve simultaneous slip on multiple steeply-dipping normal faults, then seismic signals recorded at the surface may reflect the multi-fault source and result in a higher-angle composite focal mechanism. Although our dynamic rupture models do not include multiple faults, they appear consistent with the keystone fault model. Future dynamic rupture and seismi-cycle modeling of multi-fault detachment systems could test whether dynamic stress effects may allow the keystone fault mechanism to operate at lower shear stresses, modulating interseismic slip on neighboring faults but rupturing well before being stressed to critical static frictional failure levels.

All our models assume that optimally oriented faults are close to critically stressed (R_0=0.95), which may suggest that faults better oriented than the LANF could be activated earlier in the seismic cycle than the detachment. However, our assumption is in agreement with the keystone fault model which postulates that high-angle faults cannot host large earthquakes but bleed off excess shear stress via microseismicity and/or creep. Importantly, multi-fault dynamic rupture models could explore whether any reasonable loading conditions result in LANF ruptures that do not also rupture the more steeply-dipping normal faults nearby, probing the complex rupture hypothesis for the lack of LANF focal mechanisms.

4.5 Near-surface detachment slip

Our results suggest that active detachment faults can host moderate (M_w >7) earthquakes within Andersonian stress fields and that these earthquakes may not necessarily rupture to the surface. Near-surface rupture may be impeded by the geometric effect of gentler fault dips, the stabilizing effect of clay-rich gouges, and/or the interaction of dynamic stress perturbations with the free-surface above a rupturing normal fault (Nielsen, 1998; Oglesby et al., 1998, 2000; Aochi, 2018). Additionally, model 4 considered decreased near-surface fault stress and strength conditions associated with a near-surface reduction of effective static friction f_0, testing the idea that frictionally weak gouge mineralogies may limit the magnitude of interseismic shear stresses and strains that accumulate around the shallowest parts of these faults, with excess shear stresses being relieved by shallow interseismic creep. Interseismic creep on the weak shallow portion of a mature detachment may reduce the effective shear stress there, further limiting its propensity for shallow rupture. These results are encouraging in terms of the hazard potential of detachments, as surface-rupturing earthquakes are commonly the most damaging and tsunamigenic; however, we note that our models do not include any steeply-dipping splay faults in the hanging wall, which may be better-aligned for reactivation and generate more coseismic uplift and subsidence due to their steeper geometry. Future modeling work could assess the hazard potential of complex detachment systems with splay-faulted hanging walls, while continuous high-resolution postseismic geodetic monitoring of near-fault displacements following buried rupture of a normal fault could test whether postseismic stress concentrations drive shallow afterslip updip of the rupture patch. These targeted exercises could be well-suited for another well-documented active onshore LANF, the Altotiberina fault zone in Italy, which is monitored by a dense network of geodetic and seismologic instruments (e.g., Chiaraluce et al., 2014) and exhibits mixed seismic and aseismic deformation including creep and frequent microseismicity on both the gently-dipping Altotiberina fault and steeper splay faults in its hanging wall (e.g., Chiaraluce et al., 2007; Brozetti et al., 2009; Anderlini et al., 2016; Valoroso et al., 2017).

In addition to afterslip or interseismic creep updip of the strongly locked zone, another process that may relieve shallow interseismic stress on detachments is creep on splay faults in their hanging walls, although its relative importance is unclear as such subsidiary creep is not yet geodetically well-resolved. Improved satellite geodetic capabilities of upcoming missions like NISAR (e.g., Rosen et al., 2017) could start to resolve not only interseismic creep on major plate-boundary faults but also more detailed patterns of interseismic deformation on and between minor faults nearby. These new datasets could help constrain the relative role of splay fault creep in shallow interseismic shear stress accumulation around detachment faults, which our results suggest could limit shallow coseismic slip and the associated seismic hazard of these faults.

5. Conclusions

Data-constrained dynamic rupture modeling of the Mai'iu fault indicates that subcritically stressed detachment faults dipping <30° at the surface can slip in M_w >7.0 earthquakes under Andersonian extensional stress conditions. Modeled earthquakes preferentially rupture to the surface along segments dipping more steeply near the surface, suggesting that the most shallowly dipping detachment segments are more likely to host buried ruptures that may be complemented by updip afterslip and/or interseismic creep facilitated by weak, velocity-strengthening clay-rich gouges in the shallow fault zone. At shallow depths, rupture may be limited by frictionally stable gouges, gentler fault dips, and dynamic stress interactions with the free surface.

Acknowledgments

Funding for this work was provided by a Green Postdoctoral Scholarship at the Institute for Geophysics and Planetary Physics at Scripps Institution of Oceanography and the European Union's Horizon 2020 research and innovation programme (TEAR ERC Starting grant no. 852992; ChEESE project, grant agreement No. 823844). The authors acknowledge additional funding from the German Research Foundation (DFG) (projects GA 2465/2-1, GA 2465/3-1), by KAUST-CRG (FRAGEN, grant no. ORS-2017-CRG6 3389.02) and by KONWIHR – the Bavarian Competence Network for Technical and Scientific High Performance Computing (project NewWave). Computing resources were provided by the Institute of Geophysics of LMU Munich (Oeser et al., 2006) and the Leibniz Supercomputing Centre (LRZ, project no. pr63qo). SeisSol simulations were performed on SuperMUC-NG at Leibniz-Rechenzentrum (LRZ) in Munich. We thank Carsten Uphoff and Amrit Bal for their help with SeisSol implementation and Samuel Webber for sharing the Mai'iu fault geometry model. We acknowledge helpful discussions with Samuel Webber, Marcel Mizera, Timothy Little, Carolyn Boulton, Laura Wallace, Susan Ellis, and Luc Lavier.

Open Research

The authors declare that all data supporting the findings of this study are available within the paper and its Methods section. In particular, all data required to reproduce the rupture models can be downloaded from the Zenodo repository (https://doi.org/10.5281/zenodo.6094294). We use SeisSol commit tag 2ecefa2 with branch Maiiu/f0_variable (https://github.com/SeisSol/SeisSol/tree/Maiiu/f0_variable). We use projection: +proj=tmerc +datum=WGS84 +k=0.9996 +lon_0=149.5376 +lat_0=-9.59178.

References

Abers, G. A., Eilon, Z., Gaherty, J. B., Jin, G., Kim, Y., Obrebski, M., & Dieck, C. (2016). Southeast Papuan crustal tectonics: Imaging extension and buoyancy of an active rift. *Journal of Geophysical Research: Solid Earth*, *121*(2), 951–971. https://doi.org/10.1002/2015JB012621

Abers, G. a. (2001). Evidence for seismogenic normal faults at shallow dips in continental rifts. *Geological Society, London, Special Publications*, *187*(1), 305–318. https://doi.org/10.1144/GSL.SP.2001.187.01.15

Abers, G. A. (2009). Slip on shallow-dipping normal faults. *Geology*, *37*(8), 767–768. https://doi.org/10.1130/focus082009.1.

Abers, G. A., Mutter, C. Z., & Fang, J. (1997). Shallow dips of normal faults during rapid extension: Earthquakes in the Woodlark-D'Entrecasteaux rift system, Papua New Guinea. *Journal of Geophysical Research: Solid Earth*, *102*(B7), 15301–15317. https://doi.org/10.1029/97jb00787

Ampuero, J. P., & Ben-zion, Y. (2008). Cracks, pulses and macroscopic asymmetry of dynamic rupture on a bimaterial interface with velocity-weakening friction. *Geophysical Journal International*, *173*(2), 674–692. https://doi.org/10.1111/J.1365-246X.2008.03736.X/2/173-2-674-TBL005.JPEG

Anderlini, L., Serpelloni, E., & Belardinelli, M. E. (2016). Creep and locking of a low-angle normal fault: Insights from the Altotiberina fault in the Northern Apennines (Italy). *Geophysical Research Letters*, *43*(9), 4321–4329. https://doi.org/10.1002/2016GL068604

Andrews, D. J. (1976). Rupture velocity of plane strain shear cracks. *Journal of Geophysical Research*, *81*(32), 5679–5687. https://doi.org/10.1029/JB081I032P05679

Aochi, H. (2018). Dynamic asymmetry of normal and reverse faults due to constrained depth-dependent stress accumulation. *Geophysical Journal International*, *215*(3), 2134–2143. https://doi.org/10.1093/gji/ggy407

Aochi, H., & Madariaga, R. (2003). The 1999 İzmit, Turkey, Earthquake: Nonplanar Fault Structure, Dynamic Rupture Process, and Strong Ground Motion. *Bulletin of the Seismological Society of America*, *93*(3), 1249–1266. https://doi.org/10.1785/0120020167

Aochi, H., & Twardzik, C. (2020). Imaging of Seismogenic Asperities of the 2016 ML 6.0 Amatrice, Central Italy, Earthquake Through Dynamic Rupture Simulations. *Pure and Applied Geophysics*, *177*(5), 1931–1946. https://doi.org/10.1007/s00024-019-02199-z

Aochi, H., & Ulrich, T. (2015). A probable earthquake scenario near Istanbul determined from dynamic simulations. *Bulletin of the Seismological Society of America*, *105*(3), 1468–1475. https://doi.org/10.1785/0120140283

Ariyoshi, K., Matsuzawa, T., Yabe, Y., Kato, N., Hino, R., Hasegawa, A., & Kaneda, Y. (2009). Character of slip and stress due to interaction between fault segments along the dip direction of a subduction zone. *Journal of Geodynamics*, *48*(2), 55–67. https://doi.org/10.1016/J.JOG.2009.06.001

Aslam, K. S., Thomas, A. M., & Melgar, D. (2021). The Effect of Fore-Arc Deformation on Shallow Earthquake Rupture Behavior in the Cascadia Subduction Zone. *Geophysical Research Letters*, *48*(20), 1–11. https://doi.org/10.1029/2021GL093941

Axen, G. J. (1992). Pore pressure, stress incraese, and fault weakening in low-angle normal faulting. *Journal of Geophysical Research*, *97*(B6), 8979–8991.

Axen, G. J. (2020). How a strong low-angle normal fault formed: The Whipple detachment, southeastern California. *Bulletin of the Geological Society of America*, *132*(9–10), 1817–1828. https://doi.org/10.1130/B35386.1

Axen, G. J. (2004). Mechanics of Low-Angle Normal Faults. In *Rheology and Deformation of the Lithosphere at Continental Margins*. Columbia University Press. https://doi.org/10.7312/karn12738-004

Barbot, S., Lapusta, N., & Avouac, J. P. (2012). Under the hood of the earthquake machine: Toward predictive modeling of the seismic cycle. *Science*, *336*(6082), 707–710. https://doi.org/10.1126/SCIENCE.1218796/SUPPL_FILE/BARBOT_DATA_FILE_1.PDF

Beeler, N. M., Tullis, T. E., & Goldsby, D. L. (2008). Constitutive relationships and physical basis of fault strength due to flash heating. *Journal of Geophysical Research: Solid Earth*, *113*(B1), 1401. https://doi.org/10.1029/2007JB004988

Biemiller, J., Taylor, F., Lavier, L., Yu, T.-L., Wallace, L., & Shen, C.-C. (2020). Emerged Coral Reefs Record Holocene Low-Angle Normal Fault Earthquakes. *Geophysical Research Letters*, *47*(20). https://doi.org/10.1029/2020GL089301

Biemiller, J., Boulton, C., Wallace, L., Ellis, S., Little, T., Mizera, M., … Lavier, L. (2020). Mechanical Implications of Creep and Partial Coupling on the World's Fastest Slipping Low-Angle Normal Fault in Southeastern Papua New Guinea. *Journal of Geophysical Research: Solid Earth*, *125*(10), 1–24. https://doi.org/10.1029/2020JB020117

Brozzetti, F., Boncio, P., Lavecchia, G., & Pace, B. (2009). Present activity and seismogenic potential of a low-angle normal fault system (Città di Castello, Italy): Constraints from surface geology, seismic reflection data and seismicity. *Tectonophysics*, *463*(1–4), 31–46. https://doi.org/10.1016/j.tecto.2008.09.023

Buck, W. R. (1988). Flexural Rotation of Normal Faults. *Tectonics*, *7*(5), 959–973.

Buck, W. R. (1993). Effect of lithospheric thickness on the formation of high- and low-angle normal faults. *Geology*, *21*(10), 933–936. https://doi.org/10.1130/0091-7613(1993)021<0933:EOLTOT>2.3.CO;2

Cheloni, D., De Novellis, V., Albano, M., Antonioli, A., Anzidei, M., Atzori, S., … Doglioni, C. (2017). Geodetic model of the 2016 Central Italy earthquake sequence inferred from InSAR and GPS data. *Geophysical Research Letters*, *44*(13), 6778–6787. https://doi.org/10.1002/2017GL073580

Chiaraluce, L., Chiarabba, C., Collettini, C., Piccinini, D., & Cocco, M. (2007). Architecture and mechanics of an active low-angle normal fault: Alto Tiberina Fault, northern Apennines, Italy. *Journal of Geophysical Research: Solid Earth*, *112*(10). https://doi.org/10.1029/2007JB005015

Chiaraluce, L., Amato, A., Carannante, S., Castelli, V., Cattaneo, M., Cocco, M., … Valoroso, L. (2014). The alto Tiberina near fault observatory (northern Apennines, Italy). *Annals of Geophysics*, *57*(3). https://doi.org/10.4401/ag-6426

Cochard, A., & Madariaga, R. (1996). Complexity of seismicity due to highly rate-dependent friction. *Journal of Geophysical Research: Solid Earth*, *101*(B11), 25321–25336. https://doi.org/10.1029/96JB02095

Collettini, C. (2011). The mechanical paradox of low-angle normal faults: Current understanding and open questions. *Tectonophysics*, *510*(3–4), 253–268. https://doi.org/10.1016/j.tecto.2011.07.015

Collettini, C., & Sibson, R. H. (2001). Normal faults, normal friction? *Geology*, *29*(10), 927. https://doi.org/10.1130/0091-7613(2001)029<0927:NFNF>2.0.CO;2

Cummins, P. R., Pranantyo, I. R., Pownall, J. M., Griffin, J. D., Meilano, I., & Zhao, S. (2020). Earthquakes and tsunamis caused by low-angle normal faulting in the Banda Sea, Indonesia. *Nature Geoscience*. https://doi.org/10.1038/s41561-020-0545-x

Das, S., & Aki, K. (1977). A numerical study of two-dimensional spontaneous rupture propagation. *Geophysical Journal International*, *50*(3), 643–668. https://doi.org/10.1111/J.1365-246X.1977.TB01339.X

Di Toro, G., Han, R., Hirose, T., De Paola, N., Nielsen, S., Mizoguchi, K., … Shimamoto, T. (2011). Fault lubrication during earthquakes. *Nature*, *471*(7339), 494–499. https://doi.org/10.1038/nature09838

Douilly, R., Aochi, H., Calais, E., & Freed, A. M. (2015). Three-dimensional dynamic rupture simulations across interacting faults: The Mw7.0, 2010, Haiti earthquake. *Journal of*

Geophysical Research: Solid Earth, *120*(2), 1108–1128. https://doi.org/10.1002/2014JB011595

Dunham, E. M. (2007). Conditions governing the occurrence of supershear ruptures under slip-weakening friction. *Journal of Geophysical Research: Solid Earth*, *112*(7), 1–24. https://doi.org/10.1029/2006JB004717

Dunham, E. M., Belanger, D., Cong, L., & Kozdon, J. E. (2011). Earthquake ruptures with strongly rate-weakening friction and off-fault plasticity, part 1: Planar faults. *Bulletin of the Seismological Society of America*, *101*(5), 2296–2307. https://doi.org/10.1785/0120100075

Eilon, Z., Abers, G. A., Gaherty, J. B., & Jin, G. (2015). Imaging continental breakup using teleseismic body waves: The Woodlark Rift, Papua New Guinea. *Geochemistry, Geophysics, Geosystems*, *16*(8), 2529–2548. https://doi.org/10.1002/2015GC005835

Fitz, G. (2011). *Offshore mapping and modeling of Miocene-Recent extensional basins adjacent to metamorphic gneiss domes of the D'Entrecasteaux Islands, eastern Papua New Guinea*. University of Texas at Austin.

Fitz, G., & Mann, P. (2013). Tectonic uplift mechanism of the Goodenough and Fergusson Island gneiss domes, eastern Papua New Guinea: Constraints from seismic reflection and well data. *Geochemistry, Geophysics, Geosystems*, *14*(10), 3969–3995. https://doi.org/10.1002/GGGE.20208@10.1002/(ISSN)1525-2027.LITHOS1

Fitz, G., & Mann, P. (2013). Evaluating upper versus lower crustal extension through structural reconstructions and subsidence analysis of basins adjacent to the D'Entrecasteaux Islands, eastern Papua New Guinea. *Geochemistry, Geophysics, Geosystems*, *14*(6), 1800–1818. https://doi.org/10.1002/ggge.20123

Fletcher, J. M., Oskin, M. E., & Teran, O. J. (2016). The role of a keystone fault in triggering the complex El Mayor-Cucapah earthquake rupture. *Nature Geoscience*, *9*(4), 303–307. https://doi.org/10.1038/ngeo2660

Fletcher, J. M., Teran, O. J., Rockwell, T. K., Oskin, M. E., Hudnut, K. W., Mueller, K. J., … González-García, J. (2014). Assembly of a large earthquake from a complex fault system: Surface rupture kinematics of the 4 April 2010 El Mayor-Cucapah (Mexico) Mw 7.2 earthquake. *Geosphere*, *10*(4), 797–827. https://doi.org/10.1130/GES00933.1

Gabriel, A. A., Ampuero, J. P., Dalguer, L. A., & Mai, P. M. (2012). The transition of dynamic rupture styles in elastic media under velocity-weakening friction. *Journal of Geophysical Research: Solid Earth*, *117*(9), 1–20. https://doi.org/10.1029/2012JB009468

Galis, M., Pelties, C., Kristek, J., Moczo, P., Ampuero, J. P., & Mai, P. M. (2015). On the initiation of sustained slip-weakening ruptures by localized stresses. *Geophysical Journal International*, *200*(2), 890–909. https://doi.org/10.1093/gji/ggu436

Gallovič, F., Valentová, Ampuero, J. P., & Gabriel, A. A. (2019). Bayesian Dynamic Finite-Fault Inversion: 2. Application to the 2016 Mw 6.2 Amatrice, Italy, Earthquake. *Journal of Geophysical Research: Solid Earth*, *124*(7), 6970–6988. https://doi.org/10.1029/2019JB017512

Gonzalez-Ortega, A., Fialko, Y., Sandwell, D., Nava-Pichardo, F. A., Fletcher, J., Gonzalez-Garcia, J., … Funning, G. (2014). El Mayor-Cucapah (Mw 7.2) earthquake: Early near-field postseismic deformation from InSAR and GPS observations. *Journal of Geophysical Research: Solid Earth*, *119*(2), 1482–1497. https://doi.org/10.1002/2013JB010193

Harris, R. A., Barall, M., Andrews, D. J., Duan, B., Ma, S., Dunham, E. M., … Abrahamson, N. (2011). Verifying a Computational Method for Predicting Extreme Ground Motion. *Seismological Research Letters*, *82*(5), 638–644. https://doi.org/10.1785/GSSRL.82.5.638

Harris, R. A., Barall, M., Archuleta, R., Dunham, E., Aagaard, B., Ampuero, J. P., … Templeton, E. (2009). The SCEC/USGS Dynamic Earthquake Rupture Code Verification Exercise. *Seismological Research Letters*, *80*(1), 119–126. https://doi.org/10.1785/GSSRL.80.1.119

Harris, R. A., Barall, M., Lockner, D. A., Moore, D. E., Ponce, D. A., Graymer, R. W., … Eberhart-Phillips, D. (2021). A Geology and Geodesy Based Model of Dynamic Earthquake Rupture on the Rodgers Creek-Hayward-Calaveras Fault System, California. *Journal of Geophysical Research: Solid Earth*, *126*(3), 1–28. https://doi.org/10.1029/2020JB020577

Harris, R. A., Aagaard, B., Barall, M., Ma, S., Roten, D., Olsen, K., … Dalguer, L. (2018). A suite of exercises for verifying dynamic earthquake rupture codes. *Seismological Research Letters*, *89*(3), 1146–1162. https://doi.org/10.1785/0220170222

Hayman, N. W., Knott, J. R., Cowan, D. S., Nemser, E., & Sarna-Wojcicki, A. M. (2003). Quaternary low-angle slip on detachment faults in Death Valley, California. *Geology*, *31*(4), 343–346. https://doi.org/10.1130/0091-7613(2003)031<0343:QLASOD>2.0.CO;2

Heinecke, A., Breuer, A., Rettenberger, S., Bader, M., Gabriel, A. A., Pelties, C., … Dubey, P. (2014). Petascale High Order Dynamic Rupture Earthquake Simulations on Heterogeneous Supercomputers. *International Conference for High Performance Computing, Networking, Storage and Analysis, SC*, *2015-January*(January), 3–14. https://doi.org/10.1109/SC.2014.6

Huang, Y., Meng, L., & Ampuero, J. P. (2012). A dynamic model of the frequency-dependent rupture process of the 2011 Tohoku-Oki earthquake. *Earth, Planets and Space*, *64*(12), 1061–1066. https://doi.org/10.5047/EPS.2012.05.011/FIGURES/4

Jackson, J. A., & White, N. J. (1989). Normal faulting in the upper continental crust: observations from regions of active extension. *Journal of Structural Geology*, *11*(1–2), 15–36. https://doi.org/10.1016/0191-8141(89)90033-3

Kaneko, Y., & Lapusta, N. (2010). Supershear transition due to a free surface in 3-D simulations of spontaneous dynamic rupture on vertical strike-slip faults. *Tectonophysics*, *493*(3–4), 272–284. https://doi.org/10.1016/J.TECTO.2010.06.015

Kaneko, Y., Avouac, J. P., & Lapusta, N. (2010). Towards inferring earthquake patterns from geodetic observations of interseismic coupling. *Nature Geoscience*, *3*(5), 363–369. https://doi.org/10.1038/ngeo843

Kyriakopoulos, C., Oglesby, D. D., Funning, G. J., & Ryan, K. J. (2017). Dynamic Rupture Modeling of the M7.2 2010 El Mayor-Cucapah Earthquake: Comparison With a Geodetic Model. *Journal of Geophysical Research: Solid Earth*, *122*(12), 10,263-10,279. https://doi.org/10.1002/2017JB014294

Lavier, L. L., Buck, W. R., & Poliakov, A. (1999). Self-consistent rolling-hinge model for the evolution of large-onset low-angle normal faults. *Geology*, *27*(12), 1127–1130. https://doi.org/10.1130/0091-7613(1999)027<1127:SCRHMF>2.3.CO;2

Lavier, L. L., Buck, W. R., & Poliakov, A. N. B. (2000). Factors controlling normal fault offset in an ideal brittle layer. *Journal of Geophysical Research: Solid Earth*, *105*(B10), 23431–23442. https://doi.org/10.1029/2000JB900108

Li, D., & Liu, Y. (2021). Cascadia megathrust earthquake rupture model constrained by geodetic fault locking. *Philosophical Transactions of the Royal Society A*, *379*(2196). https://doi.org/10.1098/RSTA.2020.0135

Lin, W., Byrne, T. B., Kinoshita, M., McNeill, L. C., Chang, C., Lewis, J. C., … Kanamatsu, T. (2016). Distribution of stress state in the Nankai subduction zone, southwest Japan and a comparison with Japan Trench. *Tectonophysics*, *692*, 120–130. https://doi.org/10.1016/j.tecto.2015.05.008

Lister, G. S., & Davis, G. A. (1989). The origin of metamorphic core complexes and detaehment faults formed during Tertiary eontinental margins. *Geology*, *14*(1), 246–250. https://doi.org/10.1016/0191-8141(89)90036-9

Little, T. A., Webber, S. M., Mizera, M., Boulton, C., Oesterle, J., Ellis, S., … Wallace, L. (2019). Evolution of a rapidly slipping, active low-angle normal fault, Suckling-Dayman metamorphic core complex, SE Papua New Guinea. *GSA Bulletin*. https://doi.org/10.1130/B35051.1

Liu, Y., & Rice, J. R. (2007). Spontaneous and triggered aseismic deformation transients in a subduction fault model. *Journal of Geophysical Research: Solid Earth*, *112*(9). https://doi.org/10.1029/2007JB004930

Ma, S., & Beroza, G. C. (2008). Rupture dynamics on a bimaterial interface for dipping faults. *Bulletin of the Seismological Society of America*, *98*(4), 1642–1658. https://doi.org/10.1785/0120070201

Mann, P., Horton, B. K., Taylor, F. W., Shen, C., Lin, K., Renema, W., … Renema, W. (2009). Uplift patterns of reef terraces and sedimentary rocks constrain tectonic models for metamorphic core complexes in eastern Papua New Guinea. *AGUFM*, *2009*, G33B-0642.

Mann, P., & Taylor, F. W. (2002). Emergent Late Quaternary Coral Reefs of Eastern Papua New Guinea Constrain the Regional Pattern of Oceanic Ridge Propagation. *AGUFM*, *2002*, T52C-1206.

Mann, P., Taylor, F. W., Gahagan, L., Watson, L., Mann, P., Taylor, F. W., … Watson, L. (2004). Rapid Kinematic and Tectonic Variations Along the 1400-km-long Australia-Woodlark Plate Boundary Zone, Papua New Guinea and Woodlark Basin. *AGUFM*, *2004*, T41C-1209.

McNamara, D. D., Behboudi, E., Wallace, L., Saffer, D., Cook, A. E., Fagereng, A., … Petronotis, K. E. (2021). Variable In Situ Stress Orientations Across the Northern Hikurangi Subduction Margin. *Geophysical Research Letters*, *48*(5), 1–11. https://doi.org/10.1029/2020GL091707

Melgar, D. (2021). Was the January 26th, 1700 Cascadia Earthquake Part of a Rupture Sequence? *Journal of Geophysical Research: Solid Earth*, *126*(10), e2021JB021822. https://doi.org/10.1029/2021JB021822

Melosh, H. J. (1990). Mechanical basis for low-angle normal faulting in the Basin and Range province. *Nature 1990 343:6256*, *343*(6256), 331–335. https://doi.org/10.1038/343331a0

Mizera, M., Little, T. A., Biemiller, J., Ellis, S., Webber, S., & Norton, K. P. (2019). Structural and Geomorphic Evidence for Rolling-Hinge Style Deformation of an Active Continental Low-Angle Normal Fault, SE Papua New Guinea. *Tectonics*, 2018TC005167. https://doi.org/10.1029/2018TC005167

Mizera, M., Little, T., Boulton, C., Katzir, Y., Thiagarajan, N., Prior, D. J., … Smith, E. G. C. (2021). Using Syntectonic Calcite Veins to Reconstruct the Strength Evolution of an Active Low-Angle Normal Fault, Woodlark Rift, SE Papua New Guinea. *Journal of Geophysical Research: Solid Earth*, *126*(8). https://doi.org/10.1029/2021JB021916

Mizera, M., Little, T., Boulton, C., Prior, D. J., Watson, E. J., Biemiller, J. B., … Shigematsu, N. (2020). Slow-to-Fast Deformation in Mafic Fault Rocks on an Active Low-Angle Normal Fault, Woodlark Rift, SE Papua New Guinea. *Geochemistry, Geophysics, Geosystems*. https://doi.org/10.1002/ESSOAR.10503063.1

Nielsen, S. B., & Carlson, J. M. (2000). Rupture Pulse Characterization: Self-Healing, Self-Similar, Expanding Solutions in a Continuum Model of Fault Dynamics. *Bulletin of the Seismological Society of America*, *90*(6), 1480–1497. https://doi.org/10.1785/0120000021

Nielsen, S. B. (1998). Free surface effects on the propagation of dynamic rupture. *Geophysical Research Letters*, *25*(1), 125–128. https://doi.org/10.1029/97GL03445

Niemeijer, A. R., & Collettini, C. (2014). Frictional Properties of a Low-Angle Normal Fault Under In Situ Conditions: Thermally-Activated Velocity Weakening. *Pure and Applied Geophysics*, *171*(10), 2641–2664. https://doi.org/10.1007/s00024-013-0759-6

Noda, H., Dunham, E. M., & Rice, J. R. (2009). Earthquake ruptures with thermal weakening and the operation of major faults at low overall stress levels. *Journal of Geophysical Research: Solid Earth*, *114*(7), 1–27. https://doi.org/10.1029/2008JB006143

Numelin, T., Marone, C., & Kirby, E. (2007). Frictional properties of natural fault gouge from a low-angle normal fault, Panamint Valley, California. *Tectonics*, *26*(2), n/a-n/a. https://doi.org/10.1029/2005TC001916

Numelin, T., Kirby, E., Walker, J. D., & Didericksen, B. (2007). Late Pleistocene slip on a low-angle normal fault, Searles Valley, California. *Geosphere*, *3*(3), 163–176. https://doi.org/10.1130/GES00052.1

Oeser, J., Bunge, H. P., & Mohr, M. (2006). Cluster Design in the Earth Sciences Tethys. *Lecture Notes in Computer Science (Including Subseries Lecture Notes in Artificial Intelligence and Lecture Notes in Bioinformatics)*, *4208 LNCS*, 31–40. https://doi.org/10.1007/11847366_4

Oglesby, D. D., Archuleta, R. J., & Nielsen, S. B. (2000). The three-dimensional dynamics of dipping faults. *Bulletin of the Seismological Society of America*, *90*(3), 616–628. https://doi.org/10.1785/0119990113

Oglesby, D. D., Archuleta, R. J., & Nielsen, S. B. (1998). Earthquakes on dipping faults: The effects of broken symmetry. *Science*, *280*(5366), 1055–1059. https://doi.org/10.1126/science.280.5366.1055

Oglesby, D. D., Mai, P. M., Atakan, K., & Pucci, S. (2008). Dynamic models of earthquakes on the North Anatolian fault zone under the Sea of Marmara: Effect of hypocenter location. *Geophysical Research Letters*, *35*(18), 2–5. https://doi.org/10.1029/2008GL035037

Olsen, K. B., Madariaga, R., & Archuleta, R. J. (1997). Three-dimensional dynamic simulation of the 1992 Landers earthquake. *Science*, *278*(5339), 834–838. https://doi.org/10.1126/SCIENCE.278.5339.834/ASSET/2DF981DB-6DC5-4BD4-9BB5-1299319BEC6F/ASSETS/GRAPHIC/SE4475917005.JPEG

Palgunadi, K. H., Gabriel, A. A., Ulrich, T., López-Comino, J. Á., & Mai, P. M. (2020). Dynamic fault interaction during a fluid-injection-induced earthquake: The 2017 mw 5.5 pohang event. *Bulletin of the Seismological Society of America*, *110*(5), 2328–2349. https://doi.org/10.1785/0120200106

Pelties, C., Gabriel, A. A., & Ampuero, J. P. (2014). Verification of an ADER-DG method for complex dynamic rupture problems. *Geoscientific Model Development*, *7*(3), 847–866. https://doi.org/10.5194/gmd-7-847-2014

Ramos, M. D., & Huang, Y. (2019). How the Transition Region Along the Cascadia Megathrust Influences Coseismic Behavior: Insights From 2-D Dynamic Rupture Simulations. *Geophysical Research Letters*, *46*(4), 1973–1983. https://doi.org/10.1029/2018GL080812

Ramos, M. D., Huang, Y., Ulrich, T., Li, D., Gabriel, A. A., & Thomas, A. M. (2021). Assessing Margin-Wide Rupture Behaviors Along the Cascadia Megathrust With 3-D Dynamic Rupture Simulations. *Journal of Geophysical Research: Solid Earth*, *126*(7), 1–22. https://doi.org/10.1029/2021JB022005

Rettenberger, S., Meister, O., Bader, M., & Gabriely, A. A. (2016). ASAGI - A parallel server for adaptive geoinformation. *ACM International Conference Proceeding Series*. https://doi.org/10.1145/2938615.2938618

Rice, J. R. (2006). Heating and weakening of faults during earthquake slip. *Journal of Geophysical Research: Solid Earth*, *111*(B5), 5311. https://doi.org/10.1029/2005JB004006

Rice, J. R. (1992). Chapter 20 Fault Stress States, Pore Pressure Distributions, and the Weakness of the San Andreas Fault. *International Geophysics*, *51*(C), 475–503. https://doi.org/10.1016/S0074-6142(08)62835-1

Rosen, P. A., Kim, Y., Kumar, R., Misra, T., Bhan, R., & Sagi, V. R. (2017). Global persistent SAR sampling with the NASA-ISRO SAR (NISAR) mission. *2017 IEEE Radar Conference, RadarConf 2017*, 0410–0414. https://doi.org/10.1109/RADAR.2017.7944237

Rundle, J. B., Kanamori, H., & McNally, K. C. (1984). An inhomogeneous fault model for gaps, asperities, barriers, and seismicity migration. *Journal of Geophysical Research: Solid Earth*, *89*(B12), 10219–10231. https://doi.org/10.1029/JB089IB12P10219

Shi, Z., & Day, S. M. (2013). Rupture dynamics and ground motion from 3-D rough-fault simulations. *Journal of Geophysical Research: Solid Earth*, *118*(3), 1122–1141. https://doi.org/10.1002/jgrb.50094

Sibson, R. H. (1990). Rupture nucleation on unfavorably oriented faults. *Bulletin of the Seismological Society of America*, *80*(6A), 1580–1604. https://doi.org/10.1785/BSSA08006A1580

Skarbek, R. M., & Saffer, D. M. (2009). Pore pressure development beneath the décollement at the Nankai subduction zone: Implications for plate boundary fault strength and sediment dewatering. *Journal of Geophysical Research: Solid Earth*, *114*(B7), 7401. https://doi.org/10.1029/2008JB006205

Smith, S. A. F., & Faulkner, D. R. (2010). Laboratory measurements of the frictional properties of the Zuccale low-angle normal fault, Elba Island, Italy. *Journal of Geophysical Research*, *115*(B2), B02407. https://doi.org/10.1029/2008JB006274

Spencer, J. E., & Chase, C. G. (1989). Role of crustal flexure in initiation of low-angle normal faults and implications for structural evolution of the basin and range province. *Journal of Geophysical Research: Solid Earth*, *94*(B2), 1765–1775. https://doi.org/10.1029/JB094IB02P01765

Steffen, R., & Steffen, H. (2021). Reactivation of Non-Optimally Orientated Faults Due to Glacially Induced Stresses. *Tectonics*, *40*(11). https://doi.org/10.1029/2021tc006853

Stein, R. S., & Barrientos, S. E. (1985). Planar high-angle faulting in the basin and range: Geodetic analysis of the 1983 Borah Peak, Idaho, earthquake. *Journal of Geophysical Research: Solid Earth*, 90(B13), 11355-11366. https://doi.org/10.1029/JB090iB13p11355

Thomas, M. Y., Lapusta, N., Noda, H., & Avouac, J. P. (2014). Quasi-dynamic versus fully dynamic simulations of earthquakes and aseismic slip with and without enhanced coseismic weakening. *Journal of Geophysical Research: Solid Earth*, *119*(3), 1986–2004. https://doi.org/10.1002/2013JB010615

Tinti, E., Casarotti, E., Ulrich, T., Taufiqurrahman, T., Li, D., & Gabriel, A. A. (2021). Constraining families of dynamic models using geological, geodetic and strong ground motion data: The Mw 6.5, October 30th, 2016, Norcia earthquake, Italy. *Earth and Planetary Science Letters*, *576*, 117237. https://doi.org/10.1016/j.epsl.2021.117237

Townend, J., & Zoback, M. D. (2000). How faulting keeps the crust strong. *Geology*, *28*(5), 399–402. https://doi.org/10.1130/0091-7613(2000)028<0399:HFKTCS>2.3.CO;2

Ulrich, T., Gabriel, A. A., & Madden, E. H. (2019). Coupled , Physics-Based Modeling Reveals Earthquake Displacements are Critical to the 2018 Palu , Sulawesi Tsunami. *Pure and Applied Geophysics*, *176*, 4069–4109. https://doi.org/10.1007/s00024-019-02290-5

Ulrich, T., Gabriel, A. A., Ampuero, J. P., & Xu, W. (2019). Dynamic viability of the 2016 Mw 7.8 Kaikōura earthquake cascade on weak crustal faults. *Nature Communications*, *10*(1). https://doi.org/10.1038/s41467-019-09125-w

Ulrich, T., Gabriel, A.-A., & Madden, E. H. (2022). Stress, rigidity and sediment strength control megathrust earthquake and tsunami dynamics. *Nature Geoscience 2022 15:1*, *15*(1), 67–73. https://doi.org/10.1038/s41561-021-00863-5

Uphoff, C., Rettenberger, S., Bader, M., Madden, E. H., Ulrich, T., Wollherr, S., & Gabriel, A. A. (2017). Extreme scale multi-physics simulations of the tsunamigenic 2004 sumatra megathrust earthquake. *Proceedings of the International Conference for High Performance Computing, Networking, Storage and Analysis, SC 2017*, *16*. https://doi.org/10.1145/3126908.3126948

Valoroso, L., Chiaraluce, L., Di Stefano, R., & Monachesi, G. (2017). Mixed-Mode Slip Behavior of the Altotiberina Low-Angle Normal Fault System (Northern Apennines, Italy) through High-Resolution Earthquake Locations and Repeating Events. *Journal of*

Geophysical Research: Solid Earth, *122*(12), 10,220-10,240. https://doi.org/10.1002/2017JB014607

van Zelst, I., Wollherr, S., Gabriel, A. A., Madden, E. H., & van Dinther, Y. (2019). Modeling Megathrust Earthquakes Across Scales: One-way Coupling From Geodynamics and Seismic Cycles to Dynamic Rupture. *Journal of Geophysical Research: Solid Earth*, *124*(11), 11414–11446. https://doi.org/10.1029/2019JB017539

Wallace, L. M., Ellis, S., Little, T., Tregoning, P., Palmer, N., Rosa, R., … Kwazi, J. (2014). Continental breakup and UHP rock exhumation in action: GPS results from the Woodlark Rift, Papua New Guinea. *Geochemistry, Geophysics, Geosystems*, *15*(11), 4267–4290. https://doi.org/10.1002/2014GC005458

Webber, S., Little, T. A., Norton, K. P., Österle, J., Mizera, M., Seward, D., & Holden, G. (2020). Progressive back-warping of a rider block atop an actively exhuming, continental low-angle normal fault. *Journal of Structural Geology*, *130*(May 2019). https://doi.org/10.1016/j.jsg.2019.103906

Webber, S., Norton, K. P., Little, T. A., Wallace, L. M., & Ellis, S. (2018). How fast can low-angle normal faults slip? Insights from cosmogenic exposure dating of the active Mai'iu fault, Papua New Guinea. *Geology*, *46*(3), 227–230. https://doi.org/10.1130/G39736.1

Wernicke, B. (1995). Low-angle normal faults and seismicity: A review. *Journal of Geophysical Research: Solid Earth*, *100*(B10), 20159–20174. https://doi.org/10.1029/95jb01911

Westaway, R. (2005). Active low-angle normal faulting in the Woodlark extensional province, Papua New Guinea: A physical model. *Tectonics*, *24*(6), 1–25. https://doi.org/10.1029/2004TC001744

Whitney, D. L., Teyssier, C., Rey, P., & Roger Buck, W. (2013). Continental and oceanic core complexes. *Bulletin of the Geological Society of America*, *125*(3–4), 273–298. https://doi.org/10.1130/B30754.1

Wollherr, S., Gabriel, A. A., & Mai, P. M. (2019). Landers 1992 "Reloaded": Integrative Dynamic Earthquake Rupture Modeling. *Journal of Geophysical Research: Solid Earth*, *124*(7), 6666–6702. https://doi.org/10.1029/2018JB016355

Yin, A. (1991). Mechanisms for the formation of Domal and Basinal Detachment Faults: A three-dimensional analysis. *Journal of Geophysical Research: Solid Earth*, *96*(B9), 14577–14594. https://doi.org/10.1029/91JB01113

Yin, A. (1989). Origin of regional, rooted low-angle normal faults: A mechanical model and its tectonic implications. *Tectonics*, *8*(3), 469–482. https://doi.org/10.1029/TC008I003P00469

Zheng, G., & Rice, J. R. (1998). Conditions under which velocity-weakening friction allows a self-healing versus a cracklike mode of rupture. *Bulletin of the Seismological Society of America*, *88*(6), 1466–1483. https://doi.org/10.1785/BSSA0880061466

Zoback, M. L., & Zoback, M. (2007). Lithosphere Stress and Deformation. *Treatise on Geophysics: Second Edition*, *6*, 255–271. https://doi.org/10.1016/B978-0-444-53802-4.00115-9

Zoback, M. D., & Townend, J. (2001). Implications of hydrostatic pore pressures and high crustal strength for the deformation of intraplate lithosphere. *Tectonophysics*, *336*(1–4), 19–30. https://doi.org/10.1016/S0040-1951(01)00091-9